



**Anticancer activity of a new copper (II) complex with a
hydrazone ligand. Structural and spectroscopic
characterization, computational simulations and cell
mechanistic studies on 2D and 3D breast cancer cell models**

Journal:	<i>Dalton Transactions</i>
Manuscript ID	DT-ART-03-2021-000869.R2
Article Type:	Paper
Date Submitted by the Author:	n/a
Complete List of Authors:	Balsa, Lucia; Universidad Nacional de la Plata Ferraresi, Veronica; IFLP Lavecchia, Martin; CEQUINOR Echeverría, Gustavo; UNLP, Physics Department Piro, Oscar; University of La Plata, García-Tojal , Javier; Universidad de Burgos, Quimica Pis Diez, Reinaldo; CEQUINOR - CONICET, Facultad de Ciencias Exactas, Universidad Nacional de la Plata González-Baró, Ana; National University of La Plata,, Leon, Ignacio; Universidad Nacional de la Plata,

Anticancer activity of a new copper (II) complex with a hydrazone ligand. Structural and spectroscopic characterization, computational simulations and cell mechanistic studies on 2D and 3D breast cancer cell models

Lucia M. Balsa¹, Verónica Ferraresi-Curotto^{2*}, Martin J. Lavecchia¹, Gustavo A. Echeverría², Oscar E. Piro², Javier García-Tojal³, Reinaldo Pis-Diez¹, Ana C. González-Baró¹, Ignacio E. León^{1*}

¹ Centro de Química Inorgánica (CEQUINOR, CONICET-UNLP), Facultad de Ciencias Exactas, Universidad Nacional de La Plata, Bv 120 1465, 1900 La Plata, Argentina

² Instituto de Física La Plata (IFLP, CONICET-UNLP), CC 67, B1900AVV, La Plata, Argentina

³ Departamento de Química, Universidad de Burgos, Plaza Misael Bañuelos s/n, 09001 Burgos, Spain

* ileon@biol.unlp.edu.ar, vfc@fisica.unlp.edu.ar

Abstract

We report here the synthesis, crystal structure, characterization and anticancer activity of a copper(II)-hydrazone complex, Cu(MeBH_oVa)(H₂O)₂ (for short, CuHL), against human breast cancer cells on monolayer (2D) and spheroids/mammospheres (3D). The solid-state molecular structure of the complex has been determined by X-ray diffraction methods. The conformational space was searched and geometries were optimized both in the gas phase and including solvent effects by computational methods based on DFT. The compound has been characterized in the solid state and in solution by spectroscopic (FTIR, Raman, UV-vis) methods. The results were compared with those obtained for the hydrazone ligand and complemented with DFT calculations.

Cell viability assays on MCF7 (IC₅₀(CuHL) = 1.7 ± 0.1 μM, IC₅₀(CDDP) = 42.0 ± 3.2 μM) and MDA-MB-231 (IC₅₀(CuHL) = 1.6 ± 0.1 μM, IC₅₀(CDDP) = 131.0 ± 18 μM) demonstrated that the complex displays higher antitumor activity than cisplatin (CDDP) on 2D and 3D human breast cancer cell models. Molecular docking and molecular dynamics simulations showed

that CuHL could interact with DNA, inducing a significant genotoxic effect on both breast cancer cells from 0.5 to 1 μM . On the other hand, CuHL increases the ROS production and induces cell programmed death on breast cancer cells at very low micromolar concentrations (0.5-1.0 μM). Moreover, the compound decreased the amount of breast CSCs on MCF7 and MDA-MB-231 cells reducing the percentage of CD44⁺/CD24⁻/low cells from 0.5 to 1.5 μM . In addition, CuHL overcame CDDP with an IC₅₀ value 65-fold lower against breast multicellular spheroids ((IC₅₀(CuHL) = 2.2 \pm 0.3 μM , IC₅₀(CDDP) = 125 \pm 4.5 μM). Finally, CuHL reduced mammosphere formation capacity, hence affecting the size and number of mammospheres and showing that the complex exhibits antitumor properties on monolayer (2D) and spheroids (3D) derived from human breast cancer cells.

Introduction

Cancer is one of the main causes of death worldwide ¹. In particular, breast cancer is one of the most common cancers among women with a prevalence estimated to reach 2.3 million by 2030 ². There are two types of breast cancer, ductal and lobular, which are divided into invasive and in situ (non-invasive) types, with several subtypes based on histology features. One of the most aggressive classes of breast cancer is the Triple Negative Breast Cancer (TNBC) that accounts for approximately 15% of breast cancer cases and is associated with a poor prognosis, since chemotherapy seems to be the only possible treatment, involving side effects ^{3,4}. Besides, Breast Cancer Stem Cells (BCSCs) have some particular features including self-renewal, differentiation, metastasis, migration, and treatment resistance that makes tumors more aggressive and progressive ^{5,6}. Therefore, many scientific groups are currently focusing their efforts in developing novel approaches using therapeutic agents to improve and optimize the treatment ⁷.

Metal-based drugs are a class of antitumor agents largely used in the treatment of different kinds of solid tumors including breast, colon and lung ⁸. The most successful metallodrugs are cisplatin, carboplatin and oxaliplatin, widely used in the treatment of several tumors ⁹. However, inherent or acquired resistance to platinum is one of the most relevant clinical problems in the treatment ¹⁰ and has led to an innovative research approach focusing on the anticancer activity of non-platinum-based compounds ^{11,12}.

Copper complexes show promising antitumor activity both in vitro and in vivo studies^{13–17}. Furthermore, the anti-angiogenic and anti-metastatic properties of mono-nuclear copper(II) complexes have been reported^{18,19}. Other copper complexes are cytotoxic to cancer stem cells, which are responsible for cancer relapse^{20,21}. It is important to highlight that different copper complexes are active despite their ligands not showing cytotoxic activity, a fact that evidences the central role of the metal itself in the antitumor activity^{22,23}.

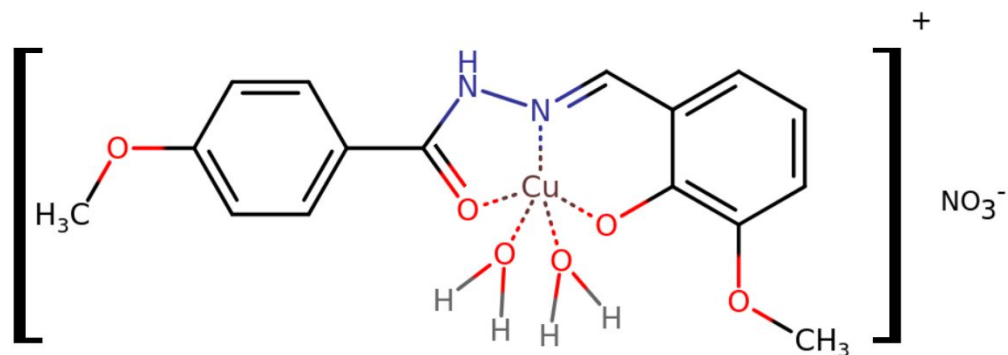
On the other hand, hydrazones and their metal complexes have attracted a remarkable interest due to their potential pharmacological activities^{24,25}. Condensation reaction of active hydrazides with some hydroxyaldehydes leads to the formation of stable hydrazones that have conserved activity, with less toxicity, due to the inactivation of NH₂ group²⁶. In particular, the reaction between 4-methoxybenzohydrazide (MeBH) with *o*-vanillin (*o*Va) forms a stable compound called MeBH*o*Va (H₂L)²⁷. Moreover, the –C=N–N–C=O group present in this kind of compounds, makes them excellent chelating agents.

As part of our study on the interaction of transition metals with hydrazones, we have synthesized a new Cu(II) coordination complex with HL and characterized it through experimental and theoretical methods. The solid-state molecular structure has been determined by single crystal X-ray diffraction. Vibration FTIR and Raman and electronic spectra were measured and the bands assigned with the aid of results from computational methods based on the Density Functional Theory (DFT). Molecular docking and molecular dynamics studies were performed with the aim to elucidate the interaction between CuHL and DNA. We report herein the anticancer activity and the mechanism of action of CuHL on breast cancer cells. We focus our research on the role of oxidative stress and its effects on apoptosis and cleavage DNA. Moreover, we studied the inhibition effect of the compound toward BCSCs. Finally, we have investigated the antitumor properties in 3D breast cancer models using spheroids and mammospheres.

Results and discussion

The molecular structure of CuHL has been determined by single crystal X-ray diffraction and fully characterized by means of vibrational spectroscopy. The compound crystallizes as a

nitrate salt of a cationic complex. As can be seen in scheme 1, the phenolic group of H₂L ligand is deprotonated, and the tridentate HL⁻ anion coordinates de Cu(II) center through the O,N,O donor set leading to a +1 charged species, with two water molecules completing the coordination environment of the metal.



Scheme 1. Schematic representation of the complex structure.

Crystal structure

Crystal data and structure refinement results are summarized in Table 1. Detailed structural data are listed as Supplementary Material (Table S1-S4).

Table 1. Crystal data and structure refinement results for CuHL.

Empirical formula	C ₁₆ H ₁₉ Cu N ₃ O ₉	
Formula weight	460.88	
Temperature	293(2) K	
Wavelength	1.54184 Å	
Crystal system	Triclinic	
Spacegroup	P-1	
Unit cell dimensions	a = 7.0729(3) Å b = 11.3899(7) Å c = 12.9557(8) Å	α = 72.750(5)° β = 75.757(5)° γ = 74.628(5)°

Volume	945.08(9) Å ³
Z, density (calculated)	2, 1.620 mg/m ³
Absorption coefficient	2.153 mm ⁻¹
F(000)	474
θ-range for data collection	3.63 to 72.40°
Index ranges	-8 ≤ h ≤ 7, -13 ≤ k ≤ 14, -16 ≤ l ≤ 15
Reflections collected	8036
Independent reflections	3713 [R(int) = 0.0329]
Observed reflections [I > 2σ(I)]	3205
Completeness to θ = 72.40°	99.6 %
Refinement method	Full-matrix least-squares on F ²
Data / restraints / parameters	3713 / 6 / 280
Goodness-of-fit on F ²	1.000
Final R indices ^a [I > 2σ(I)]	R1 = 0.0465, wR2 = 0.1329
R indices (all data)	R1 = 0.0536, wR2 = 0.1444
Largest diff. peak and hole	0.642 and -0.404 e.Å ⁻³

$$^a R_1 = \frac{\sum ||F_o| - |F_c||}{\sum |F_o|}, wR_2 = \frac{[\sum w(|F_o|^2 - |F_c|^2)^2 / \sum w(|F_o|^2)^2]}{1/2}$$

Figure 1 is an ORTEP²⁸ drawing of the complex, and corresponding intramolecular bond distances and angles around copper ion are listed in Table 2. The compound crystallizes as a complex cation with +1 charge, [Cu(HL)(H₂O)₂]⁺, and nitrate as a counterion. The Cu(II) ion is in a distorted square pyramidal coordination with a HL⁻ deprotonated hydrazone at the pyramid basis acting as a tridentate ligand through its phenoxo and carbonyl oxygen atoms [C-O bond distances of 1.889(2) Å and 1.966(2) Å] and the imine N-atom [d(Cu-N) = 1.930(2) Å], nearly along their respective electron lone-pair lobes [Cu-L-C (L: O, N) bond angles in the 113.3(2)-

128.1(2)° range]. The pyramid basis is completed with a water molecule [$d(\text{Cu-Ow}) = 1.975(2)$ Å] that binds the metal along the bisector of the oxygen lone-pair lobes (Cu-Ow-H angles of about 124°) and a second water molecule is at the pyramid apex [$d(\text{Cu-Ow}) = 2.318(2)$ Å], making a much weaker bond to the metal along one of the oxygen lone-pair lobes (Cu-Ow-H angles of about 105°). The crystallographic results indicate for the copper unpaired electron (or hole) ground state a mainly $d(x^2-y^2)$ orbital.

Because of extended π -bonding, the HL⁻ ligand is planar [*rms* deviation of atoms from the best least-square plane is less than 0.07 Å] with the metal close onto the plane [at 0.059(1) Å].

The lattice is further stabilized by a network of NH \cdots O(nitrate), OwH \cdots O(nitr), OwH \cdots O(carb), OwH \cdots O(metx), and OwH \cdots Ow intermolecular bonds. Corresponding H-bond distances and angles are detailed in Table S5 (Supplementary material).

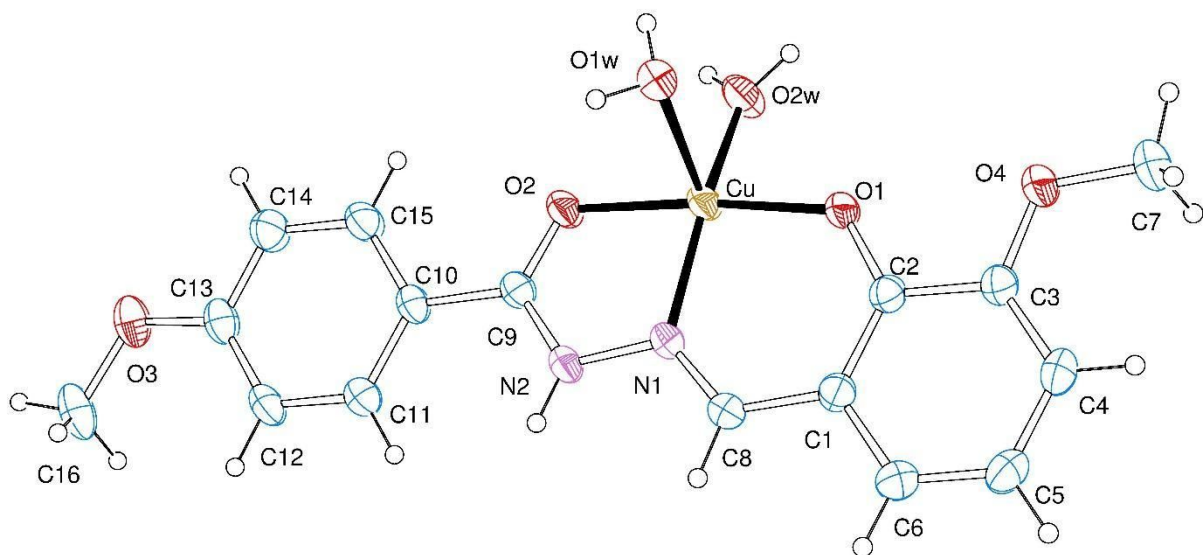


Figure 1. View of $[\text{Cu}(\text{HL})(\text{H}_2\text{O})_2]^+$ complex showing the labeling of non-hydrogen atoms and their displacement ellipsoids at the 30% probability level.

Table 2. Bond lengths [Å] and angles [°] around copper(II) for CuHL.

Bond lengths [Å]		
	Experimental	Calculated*
N(1)-Cu	1.930(2)	2.114
O(1)-Cu	1.889(2)	1.904
O(2)-Cu	1.966(2)	2.019
O(1W)-Cu	2.318(2)	---
O(2W)-Cu	1.975(2)	---

Bond angles [°]		
O(1)-Cu-N(1)	93.51(9)	91.2
O(1)-Cu-O(2)	174.44(8)	169.4
N(1)-Cu-O(2)	81.10(9)	78.2
O(1)-Cu-O(2W)	91.61(9)	---
N(1)-Cu-O(2W)	158.4(1)	---
O(2)-Cu-O(2W)	92.93(9)	---
O(1)-Cu-O(1W)	90.75(9)	---
N(1)-Cu-O(1W)	107.75(9)	---
O(2)-Cu-O(1W)	92.20(9)	---

* Water molecules and counterion are not taken into account in calculations.

Vibrational spectroscopy

The solid-state vibrational properties of the hydrazone (H₂L) and its copper complex were explored. A detailed comparative analysis of the obtained spectra, shown in Figure 2, was done. The spectral assignments were done based on reported data^{27,29,30} and with the aid of calculated normal modes, complete IR and Raman spectroscopic analysis is summarized in Table S6 (Supplementary material). H₂L data previously reported by our group (already published in²⁷) and calculated data for the complex, are included. A good agreement is found between experimental and calculated frequencies.

The IR spectrum of the copper compound shows a medium broad band, corresponding to the characteristic stretching modes of coordinated water at 3396 cm⁻¹. It is observed that the band assigned to NH stretching mode is red-shifted in comparison to the uncoordinated ligand. As

it is seen in Table S6, NH group participates in a hydrogen bond with the oxygen of the nitrate ion [N-H...O(NO₃)], this results in an overestimation of the calculated N-H stretching frequency with respect to the experimental one, as H-bond interactions are neglected in the calculations. Stretching OH mode corresponding to the free ligand is not observed in either spectra (Raman or infrared) upon coordination, nor are the bands related to the in-plane and out-of-plane OH bending modes, as expected. Several bands calculated in between 3232 cm⁻¹ and 3000 cm⁻¹ and seen in between 3100 cm⁻¹ and 2800 cm⁻¹ and can be mainly assigned to in-phase and out-of-phase stretching of the CH in the rings and characteristic modes of the methoxyl groups of the ligand. A very weak band is observed at 1767 cm⁻¹ in the infrared spectra of the copper complex, which is assigned to $\nu_1 + \nu_4$ of the nitrate counterion, in agreement with X-ray findings^{31,32}. The strong band observed at 1607 cm⁻¹ in the infrared spectra and at 1609 cm⁻¹ in the Raman spectra, is calculated at 1688 cm⁻¹ and related to the C=O and C=N stretching coupled with the stretching on *o*Va ring. This is in accordance with the crystallographic results and previous findings²³. It is also observed that this vibrational mode is conserved upon complexation of the ligand. Moreover, a medium band is found in the complex spectrum, corresponding to the stretching of the C-O involved in the coordination to the metal center, at 1538 cm⁻¹ (infrared) and 1543 cm⁻¹ (Raman). Water molecules in the solid structure interact with the oxygen atom in this C=O bond (Figure 1), but are not included in the calculations, so this frequency is overestimated and predicted at 1648 cm⁻¹. NH bending mode, that is observed in the Raman spectrum, as a sole band at 1494 cm⁻¹, is calculated at 1550 cm⁻¹ and appears coupled with other vibrations at lower frequencies in the infrared spectrum (1319 and 1304 cm⁻¹). In addition, the strong band found at 1384 cm⁻¹ and 1390 cm⁻¹ in infrared and Raman spectra of the complex, respectively, is assigned to ν_3 mode of the nitrate counterion, coupled with the stretching mode of the Ar-O group of the aldehyde fragment. Furthermore, two other copper involved vibrations are found around 640 cm⁻¹ for both spectroscopies, assigned to δ of the coordination ring (see Table S6). Cu-O stretching is observed in the infrared spectra at 546 cm⁻¹, Cu-O1 is calculated at 570 cm⁻¹ whereas Cu-O2 is calculated at 541 cm⁻¹. Moreover, γ NH is conserved after complexation.

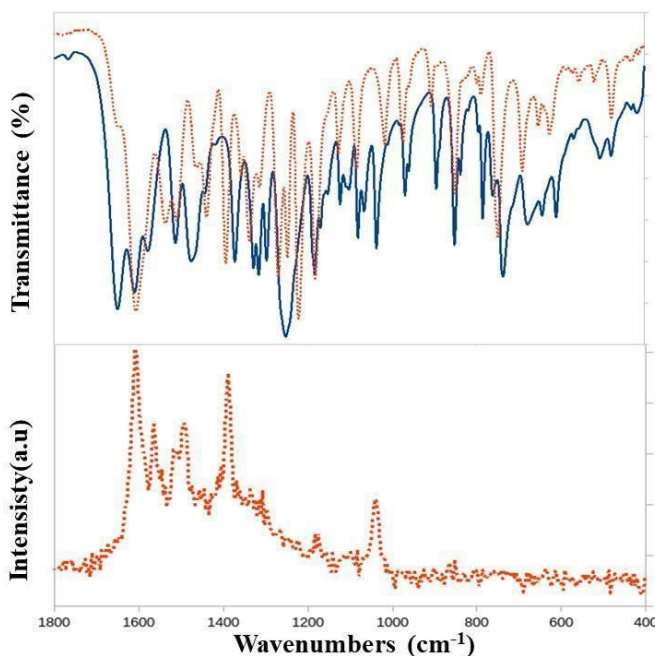


Figure 2. Experimental IR (top) and Raman (bottom) spectra of H₂L (solid) and CuHL (dotted) in the 1800-400 cm⁻¹ range.

Electronic spectroscopy

Electronic absorption spectra of the Cu(II) complex and its ligand were measured in the 200-800 nm region, on methanolic 3x10⁻⁵ M solutions. In order to observe the *d-d* band, a more concentrated (1x10⁻³ M) methanolic solution of the complex was also measured. In Table S7 most significant experimental absorption bands and calculated electronic transitions of CuHL are listed, together with the proposed assignments. Figures of the molecular orbitals involved in the electronic transitions are also available as supplementary material (Figure S1). The assignments were accomplished within the framework of TD-DFT. Nitrate ions were not taken into account in the calculations. It can be seen from the table that most transitions must be described by two or more mono-electronic excitations, which, in turn, involve many molecular orbitals. Figure 3 shows the UV-vis spectrum of the studied copper complex in comparison with the spectrum of the uncoordinated ligand (already published in ²⁷), an insight of a region of interest in the spectrum of the more concentrated solution is also

inserted. It can be observed in Figure S1 that both HOMO and HOMO-1 are localized in *o*Va ring, its -OCH₃ and the coordination sphere, whereas HOMO-2 and HOMO-7 are strongly delocalized in the *o*Va fragments, the two N atoms, MeBH moiety and the copper atom. HOMO-4 and HOMO-6 are mostly situated in copper atoms and MeBH rings and its -OCH₃ substituent. LUMO and LUMO+1 are localized in both *o*Va and MeBH rings, nitrogen atoms but neither the copper atom nor the -OCH₃ substituents of the aromatic rings are involved. LUMO+5 is localized on the copper, atom, the *o*Va ring and its -OCH₃ substituent. LUMO+6 is localized only on *o*Va aromatic ring.

Taking both the MO description given above and the results shown in Table S7 into account, it can be concluded that the bands observed at 230 and 290 nm can be assigned to intra-ligand processes, which are described by the calculated transitions at 251 and 256 nm and 279 nm, respectively. Those transitions also show a small contribution from ligand to metal charge transfer processes. On the other hand, the bands observed at 322 nm and 402 nm are described by calculated transitions at 306 nm and 334 and 340 nm, respectively. Those transitions are assigned to ligand to metal charge transfer processes. The broad and less intense band with maximum at 710 nm involves the less energetic characteristic *d-d* transitions of the Cu(II) ion in a distorted square pyramidal environment and it can be described by the calculated transition at 572 nm. This absorption, already observed in a very closely related compound²³, involves the expected transitions for the described Cu(II) species, denoting its presence in solution.

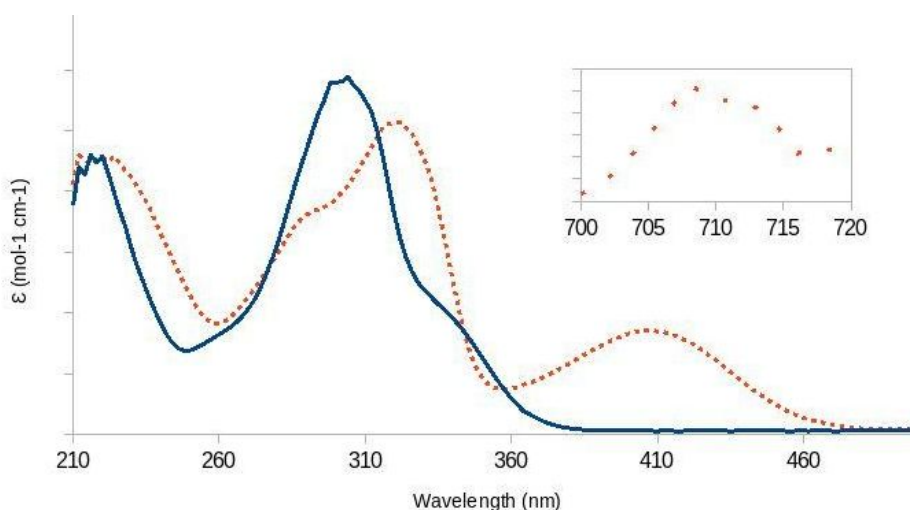


Figure 3. Electronic absorption spectra of the complex (dotted line) and the free ligand (solid line), in MeOH (3×10^{-5} M), in the 210-550 nm spectral range. Inset: Higher concentration (5×10^{-3} M) was employed to register d–d transition.

EPR spectroscopy

The X-band EPR spectrum of CuHL at RT (Figure 4) is characteristic of a dx^2-y^2 ground-state, with $g_1 = 2.278$, $g_2 = 2.072$ and $g_3 = 2.053$, in accordance with the crystallographic results. The G-value³³ is 4.45, (Equation 1), which suggests negligible magnetic exchange interactions, in good agreement with the monomeric character of the paramagnetic centres. Therefore, the g -values are meaningful in order to calculate the predominant magnetic orbital contribution in the ground state. Thus, for a given $g_1 < g_2 < g_3$ sequence, the calculated parameter R (Equation 2) is 0.09. Note that R -values < 1 are characteristic of a dx^2-y^2 ground-state³³⁻³⁴. These results agree well with the square-pyramidal geometry deduced by the Addison's parameter³⁵ from the crystallographic data, $\tau = (O1-Cu-O2 - N1-Cu-O2w) / 60 = 0.27$.

$$G = \frac{(g_{\parallel} - 2)}{(g_{\perp} - 2)} \quad \text{(Equation 1)}$$

$$R = \frac{(g_2 - g_1)}{(g_3 - g_2)} \quad \text{(Equation 2)}$$

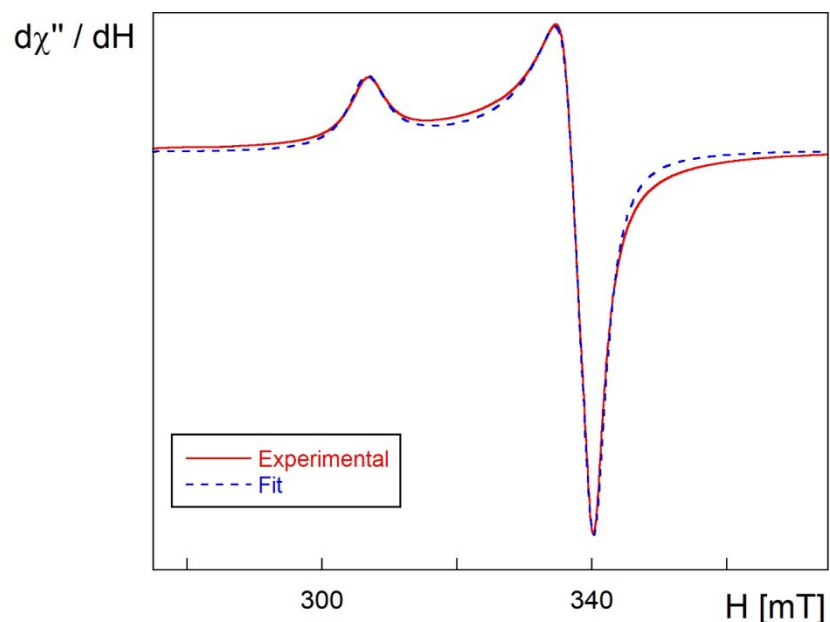


Figure 4. EPR spectrum at 298 K (solid line) together with the best fit (dashed line).

Cytotoxicity and cell proliferation studies

Cytotoxicity studies were determined by the MTT assay for complex, ligand and free cation with MCF7 (breast adenocarcinoma), MDA-MB-231 (triple negative breast adenocarcinoma), A549 (lung adenocarcinoma), MG-63 (human osteosarcoma), HT-29 (colorectal adenocarcinoma), L929 (mouse non-tumoral fibroblast) and MCF10 (non-tumoral mammary gland) cells. Clinical agent cisplatin was used as clinical reference.

Table 3 shows that CuHL diminished the cell viability in the sub micromolar range of concentration (0.5-2 μM) for human breast, lung and bone cancer cells showing the lowest IC_{50} values on breast cancer cells ($p < 0.01$). Besides, this compound reduced the cell viability in the low micromolar range (5-15 μM) for human colorectal cancer cells ($p < 0.01$). Moreover, it is important to highlight that the compound is more active than cisplatin (CDDP) in all the tested cell lines showing an IC_{50} value 25-fold lower on MCF7 and significantly 82-fold lower on MDA-MB-231 cells. In addition, the IC_{50} values of CuHL on MCF and MDA-MB-231 are comparable with the clinical drug reference doxorubicin³⁶.

On the other hand, the IC_{50} values of the ligand (H_2L) and $\text{Cu}^{(+2)}$ (free metal cation) are greater than 100 μM for both cell lines tested, hence revealing the key role of complexation

to modulate the anticancer activity of CuHL. This kind of effect has been reported for other copper complexes and other metal-based compounds^{23,37,38}.

To comprehend the potential of CuHL and to know its selectivity for tumor cells, we explored its impact on the cell viability of L929 cells (mouse derived fibroblasts) and MCF10 (non-tumoral breast cancer cells) we compared their effects by calculating the selectivity index (SI= IC₅₀ non-tumoral cells / IC₅₀ tumor cells).

The results show that CuHL has great selectivity for breast cancer cells showing SI values of 2.6 and 2.8 for MCF7 and MDA-MB-231, respectively. In this sense, the compound improved the selectivity values than cisplatin in all the cancer cell lines tested.

Several scientific evidence showed that copper complexes with IC₅₀ values lower than 10 μM have been recognized as potent cytotoxic agents against different human cancer cell lines^{13,15}. Considering the type of ligand used in this work we find that Low *et al* reported the anticancer activity of novel Cu(II) complex with the Schiff base N0-[1-(2-oxo-2H-chromen-3-yl)-ethylidene]-hydrazinecarbodithioic acid benzyl ester on MDA-MB-231 and MCF-7 cells showing IC₅₀ values around of 20 μM³⁹. Besides, four copper(II) complexes with vanillin Schiff base derivatives and naproxen were synthesized by Lu *et al*. The most effective complex showed a good cytotoxicity against bulk breast cancer cells and breast cancer stem cells, with a medium micromolar cytotoxicity (37.6 ± 3.3 and 36.0 ± 4.6 μM respectively)⁴⁰.

On the other hand, copper(II) complex of S-methyldithiocarbamate with isatin were synthesized and screened for cytotoxic activities against breast cancer cell lines (MCF7 and MDA-MB-231). The complex exhibited marked and selective activity against MCF7 cell with an IC₅₀ value in the low micromolar range (0.45 μM)⁴¹. In addition, Gou *et al*. synthesized a Cu(II) complex derived from tridentate (E)-N'-(5-bromo-2-hydroxybenzylidene) benzohydrazide Schiff base ligand, [Cu(L)(Ind)NO₃] that showed an important cytotoxicity against doxorubicin-sensitive and -resistant MCF-7 (IC₅₀ = 1.5 μM) and MCF-7/ADR cells (IC₅₀ = 1.8 μM)⁴².

Table 3. IC₅₀ (μM) values of the CuHL and CDDP in several cell lines after 24 h of incubation. ND: not determined.

	IC₅₀ CuHL	IC₅₀ CDDP
MCF7	1.7 ± 0.1	42 ± 3.2
MDA-MB-231	1.6 ± 0.1	131 ± 18
A549	2.8 ± 0.7	114 ± 2.3
MG-63	2.6 ± 0.3	39 ± 1.8
HT-29	9.7 ± 0.5	191 ± 2.6
L929	4.2 ± 0.1	11.2 ± 1.6
MCF10	4.5 ± 0.8	ND

Due to high selectivity of the compound toward breast cancer cell lines we continue the study of mechanism of action using MCF7 and MDA-MB-231.

To evaluate the effect of the complex on the cellular reproductive potential, a clonogenic assay was performed.

Figure 5 shows a strong reduction of cell proliferation on MCF7 and MDA-MB-231 cells. affecting the colony formation in a dose-dependent manner from 0,1-0.5 μM (p<0.01). These results agree with the cell viability assay.

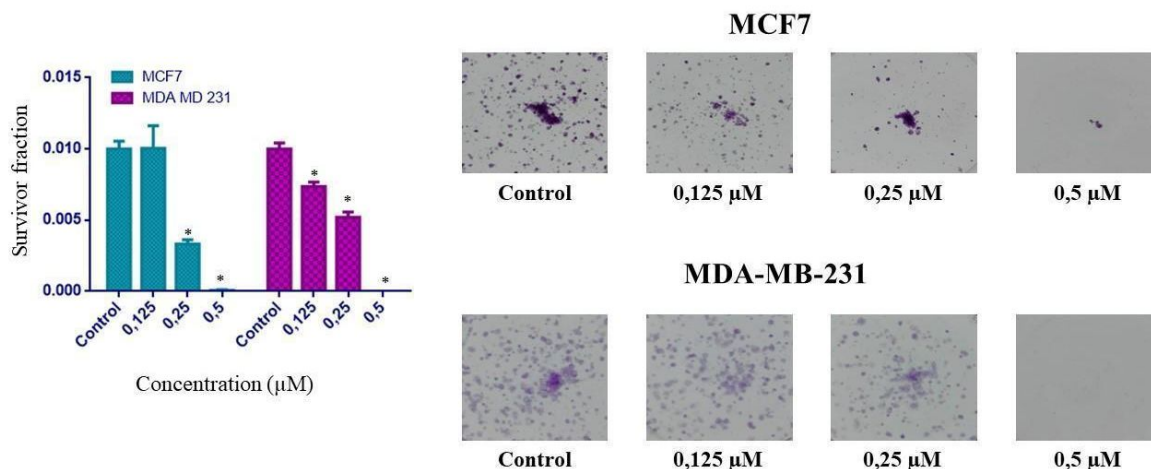


Figure 5. Clonogenic assay. Effect of CuHL on MCF-7 and MDA-MB-231 cell viability. Cells were incubated in Dulbecco's modified Eagle's medium (DMEM) alone (control) or with different concentrations (0.125, 0.25 and 0.50 μM) of compound. The results are expressed as surviving fraction as the percentage of the basal level and represent the mean \pm the standard error of the mean (SEM) ($n=18$). * $p < 0.01$ differences between control and treatment.

DNA interaction studies

Molecular docking

Molecular docking was carried out to find and score binding pose of the metal complex on DNA. The best pose of the metal complex with DNA fragments was selected based on HEX scores, (see Figure 6A). To avoid edge effects, it was considered that the complex location was not very close to the ends of the DNA dodecamer. The results showed that the metal complex was located in a minor groove of the DNA dodecamer.

Molecular dynamics and binding energy

Molecular dynamics is a computational tool to simulate the motions of a molecular system. The method requires an interaction potential from which interatomic forces can be calculated and the equations of motion that govern the dynamics of the system are determined. Molecular dynamics simulation studies were then performed to study in more details the binding modes of this metal complex. RMSD values were depicted to determine the convergence and stability of simulations (Figure S2).

The binding energy based on the molecular dynamic's trajectory was calculated with MM/GBSA model (-48 ± 7 kcal mol⁻¹) and decomposition energies are shown in Figure S3. This shows that the major interactions correspond to nucleotides surrounding copper, in particular with the nucleotides DA5, DA6, DC21, and DG22. Details of the interactions of CuHL with dodecamer are shown in Figure 6B.

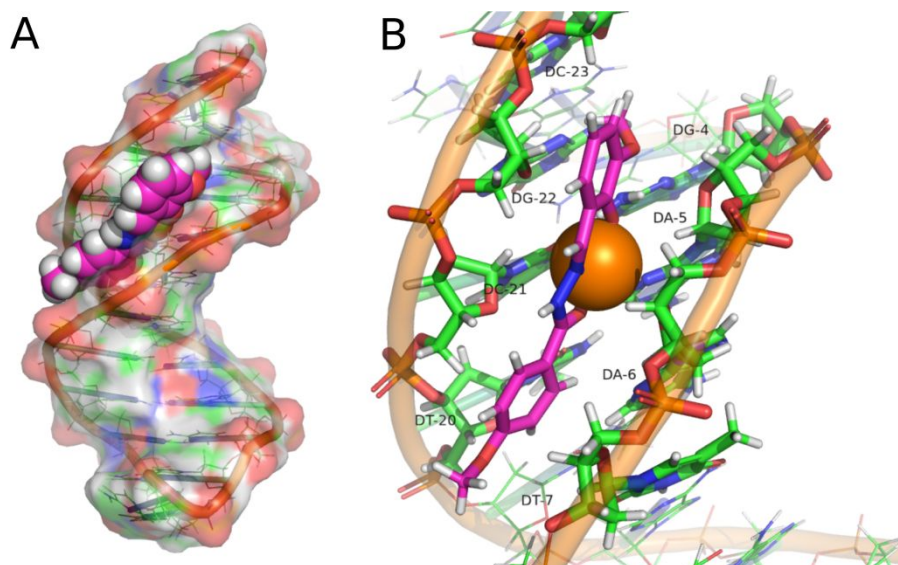


Figure 6. A) The best pose of complex (cyan sticks) obtained by molecular docking using HEX. B) Interaction details of complex (cyan) with dodecamer. Both Images are generated with Pymol (<https://pymol.org/>).

Genotoxic studies

The genotoxic effect of CuHL was performed through the induction of DNA damage. The comet assay is a valuable test used to evaluate genotoxicity.

We evaluated the tail moment parameter, which is defined as the tail length \times DNA amount in the tail ⁴³.

Figure 7 shows that complex induced a significant genotoxic effect in both breast cancer cells from 0.5 to 1 μ M with a dose–response effect ($p < 0.01$).

Moreover, the genotoxic effects of the complex are higher than cisplatin showing following tail moment values on MCF7 cells: 43.7 ± 6.0 (0.5 μ M complex), 82.2 ± 7.1 (1.0 μ M complex) and 2.4 ± 0.7 (0.5 μ M CDDP) 2 ± 0.5 (1.0 μ M CDDP). Besides, on MDA-MB-

231 cells, the compound increased the DNA damage whilst cisplatin did not exert genotoxic effects at 0.5 and 1.0 μM ($p < 0.01$).

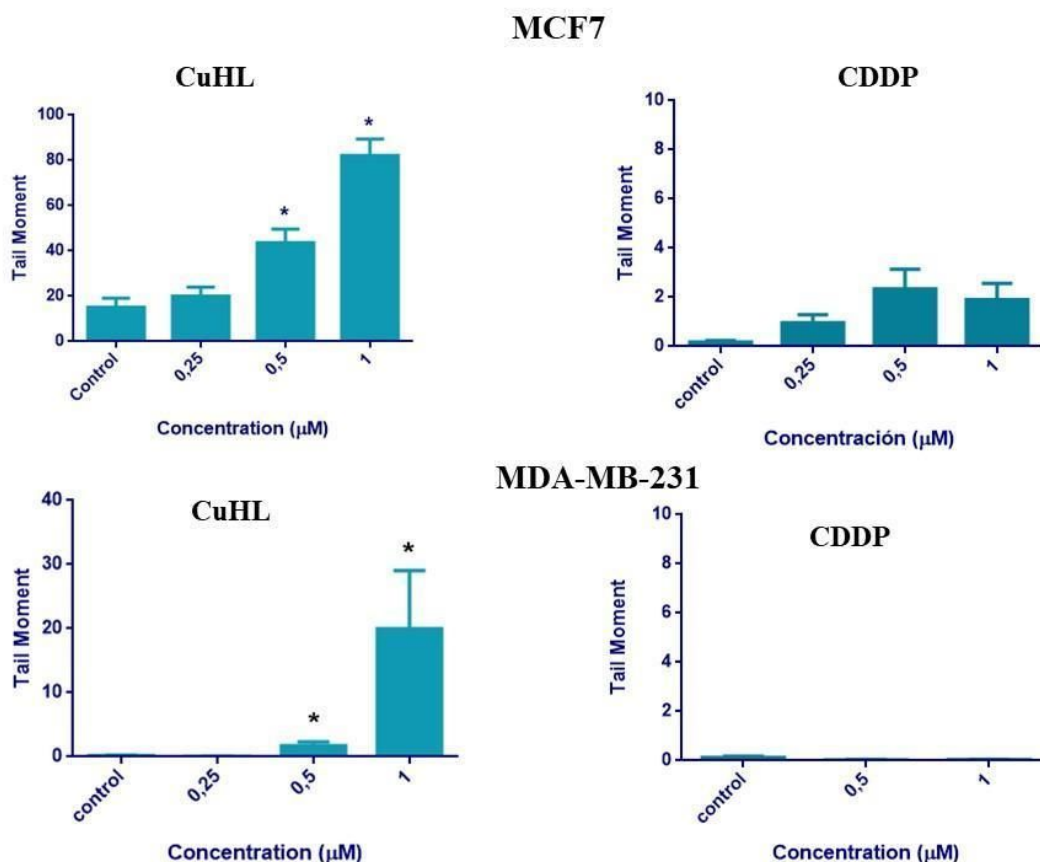


Figure 7. Genotoxicity of CuHL toward MCF7 and MDA-MB-231 cancer cells by Comet assay. After incubation with CuHL for 24 h, cells were lysed and DNA fragments were processed by electrophoresis. After electrophoresis, the nuclei were stained and analyzed. The results are expressed as the mean \pm SEM ($n = 150$).

* $p < 0.01$ differences between control and treatment.

ROS production

Copper(II) complexes can initiate Fenton reactions intracellularly resulting in ROS accumulation⁴⁴. Many scientific reports establish a relationship between anticancer activity and the redox potentials of the copper(II) complexes. The reduction of Cu(II) to Cu(I) occurs in the presence of the intracellular thiols, such as glutathione (GSH), generating a depletion

of GSH levels⁴⁵. Upon reaction with molecular oxygen, Cu(I) is reoxidized to Cu(II) thereby producing reactive superoxide radicals ($O_2^{\cdot -}$)^{46,47}.

For a better understanding of the possible mechanism involved in the cytotoxicity of CuHL on breast cancer cells, we investigated the effect of oxidative stress through the oxidation of the probes Dihydroethidium (superoxide indicator)⁴⁸.

The results evidenced that CuHL (1 μ M) caused an increment in ROS production of 720% and 1400% over basal for MDA-MB-231 and MCF7, respectively. These results suggest that ROS production could be considered as one of the relevant mechanisms of action of CuHL. In this sense, many authors demonstrated that copper(II) complexes induce cell death associated with ROS generation and depletion of cellular glutathione⁴⁹. Since then various copper(II) complexes were shown to readily react with GSH and induce oxidative stress⁵⁰.

Apoptosis

Apoptosis is a physiological process of cell death enhanced in the presence of injurious agents⁵¹. Consequently, a genetic program that leads to cell death is activated. Independently of the cell type⁵¹ and the nature of the harmful agent, the externalization of phosphatidylserine is always present in the earlier apoptotic events. Annexin V-FITC is a fluorescent probe with high affinity for phosphatidylserine, allowing its determination by fluorescence assays.

Table 4 and Figure S4 displayed the flow cytometry results of the apoptotic process in the presence of CuHL (0.25, 0.5, 0.75 and 1.0 μ M) on MCF7 and MDA-MB-231 cells.

CuHL increased the late apoptotic (Annexin V+/PI+) cell fractions from 0.25-1.0 μ M for MCF7 and the early (Annexin V+/PI-) and late apoptotic (Annexin V+/PI+) cell fractions from 0.75-1.0 μ M for MDA-MB-231 cells.

On MCF7 cells, the basal condition showed 5% of V+/PI+ cells but these results changed with the compound incubation, showing a significant increase in the late apoptotic cellular fraction (51% at 0.75 μ M, 70% at 1.0 μ M).

On the other hand, on MDA-MB-231 cells, the basal condition showed 1 % of V+/PI- cells and 2% of V+/PI+ cells whilst after incubation with 0.75 μ M of complex these values increased until 19% and 26%, respectively. At 1 μ M, CuHL resulted on 14% of V+/PI- cells and 42% of V+/PI+ cells cells,

Our results are in agreement with the cell viability studies, suggesting that CuHL induced the cell apoptosis depended on its concentration in both breast cancer cell lines. It is important to highlight that the apoptosis cell death have also been reported as the leading mechanism of action for many copper complexes with antitumor activity toward different cancer cell lines ¹⁵.

Table 4 Percentage of apoptotic cells treated with CuHL. *p < 0.01 differences between control and treatment.

	MCF7 cells		MDA-MB-231	
Concentration (μM)	V+/ PI- cells	V+/ PI+ cells	V+/ PI- cells	V+/ PI+ cells
0	1.9 ± 0.6	4.9 ± 2.1	1.4 ± 0.2	2.1 ± 0.3
0.25	5.0 ± 2.1	8.2 ± 1.7*	1.5 ± 0.1	3.1 ± 0.1
0.5	3.1 ± 1.0	28.0 ± 5.5*	2.4 ± 0.2	4.9 ± 0.2
0.75	2.3 ± 0.8	50.8 ± 2.5*	19.1 ± 1.5*	25.9 ± 3.4*
1.0	4.7 ± 1.1	70.4 ± 6.9 *	14.0 ± 0.7*	42.4 ± 2.4*

Cancer stem cell studies

Solid tumors are made up of heterogeneous cancer cell populations with different hierarchical pattern ⁵². In this sense, cancer stem cells (CSCs) are an immortal subgroup within the total malignant cell population with the potential to accumulate mutations to promote the tumor development ⁵³. CSCs play a key role in tumor aggressiveness, due to the self-renewal and the stemness capacity ⁵⁴. Therefore, in the last years, the development of anti-CSC-agents had great attention and the CSCs became an important and specific cell target ⁵⁵.

In order to evaluate the anti-CSCs activity of CuHL, we performed flow cytometry experiments using CD44 and CD24 antibodies. The breast CSC subpopulation CD44⁺/CD24⁻

with described tumorigenic capacity which originated the heterogeneity of the parental tumor ⁵⁶.

Table 5 and Figure S5 depicted that the complex decreased the amount of breast CSCs on MCF7 and MDA-MB-231 cells. On MCF7, complex reduced the percentage of CD44⁺/CD24⁻ cells showing the following values: 1.7 % (basal condition), 1.0 % (0.5 μ M), 0.5 % (1.0 μ M) and 0.3% (1.5 μ M). Besides, on MDA-MB-231 cells the basal condition resulted on 98.6 % CD44⁺/CD24⁻ whilst this value is extremely reduced after incubation with compound displaying 85.6 % (1.0 μ M) and 68.3% (1.5 μ M), respectively. In addition, the percentages of CSCs are higher on MDA-MB-231 than MCF7 cells.

Table 5 Percentage of CD 44⁺/ CD24⁻ MDA-MB-231 and MCF7 cells after treatment with 0, 0.5, 1, 1.5 μ M of CuHL. *p < 0.01 differences between control and treatment.

	% CD 44⁺/ CD24⁻ MCF7 cells	% CD 44⁺/ CD24⁻ MDA-MB-231 cells
0	1.63 \pm 0.08	98.10 \pm 0.45
0.5	0.88 \pm 0.14 *	98.34 \pm 0.12
1	0.44 \pm 0.06 *	87.44 \pm 1.86 *
1.5	0.35 \pm 0.09 *	74.61 \pm 6.29 *

3D studies: cell viability and cell proliferation

For many years, 2D cell culture has been used to study breast cancer. Nevertheless, in last 10 years, the importance of 3D culture to demonstrate the complexity of human disease has received attention, so several clinically relevant models have developed and implemented a to study breast cancer ⁵⁷.

To verify the anticancer activity of complex, we evaluated CuHL and cisplatin effects on the cell viability of MCF-7 multicellular spheroids using resazurin reduction assay.

The results showed the IC_{50} value for CuHL is $2.2 \pm 0.3 \mu\text{M}$ while for CDDP is $125 \pm 4.5 \mu\text{M}$ on spheroids derived from MCF7 cells showing an evident greater anticancer activity than cisplatin. The complex exhibited an IC_{50} value 57-fold lower than CDDP against breast multicellular spheroids. It is relevant to mention that IC_{50} values of complex on 2D and 3D cell models are close similar ($IC_{50(2D)} = 1.7$ vs $IC_{50(3D)} = 2.2$) confirming the potential application of this copper compound in breast cancer treatment. Besides, as it can be seen in Figure 8A, the complex diminished the cell viability affecting the shape and volume of the spheroids.

To confirm the anticancer potency of the complex on the 3D cell model we performed a clonogenic assay. Figure 8B shows that the compound reduced the colony formation in a dose-dependent manner ($p < 0.01$). The basal condition ($0 \mu\text{M}$) showed the formation of 160.0 ± 7.2 colonies whilst this value was reduced until 102.0 ± 3.0 colonies and 39.7 ± 2.3 colonies for 2.5 and 10 μM , respectively ($p < 0.01$). On the other hand, Figure 7C shows that the compound reduced the spheroid spreading in a dose-dependent manner from 1 to 5 μM ($p < 0.01$).

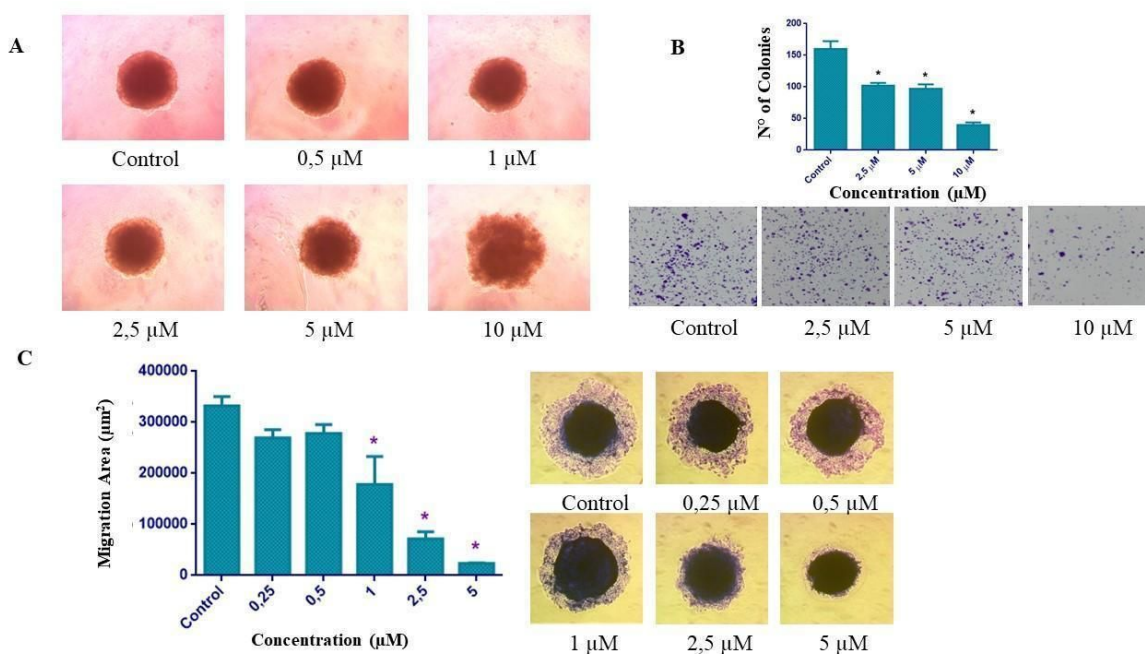


Figure 8. Effect of CuHL on MCF-7 spheroids **A)** Images of spheroids after the treatment with 0.5-10 μM of CuHL **B)** Clonogenic assay of spheroids. Spheroids were incubated in Dulbecco's modified Eagle's medium (DMEM) alone (control) or with different concentrations (2.5, 5.0 and 10.0 μM) of compound. The results are expressed as a surviving fraction as the percentage of the basal level and represent the mean \pm the standard error of the mean (SEM) (n =18). *p < 0.01 differences between control and treatment. **C)** Spreading of spheroids. Spheroids were incubated in Dulbecco's modified Eagle's medium (DMEM) alone (control) or with different concentrations (0.25-5 μM) of compound. The results are expressed as a migration area and represent the mean \pm the standard error of the mean (SEM) (n =18). *p < 0.01 differences between control and treatment.

3D studies: mammospheres forming capacity

Mammospheres are tumor-like three-dimensional structures composed of a high proportion of breast cancer stem cells (BCSCs) ⁵⁸. In this sense, the ability of the metal-based drugs to inhibit mammosphere formation from single-cell suspensions provides a reliable marker for CSC potency ⁵⁹.

Figure 9 shows that CuHL diminishes the formation and size of MCF7 mammospheres from 0.5 to 1 μM (p < 0.01). At 0.5 μM , complex reduced the mammospheres formation efficiency by 40% whilst at 1 μM the compound appreciably decreased this efficiency until 75% (*p < 0.01). Besides, as it can be seen in Figure 8, the size and number of mammospheres formed was also remarkably reduced in a dose dependent manner by CuHL.

In this sense, many copper(II) complexes with heterocycles and Schiff base ligands reduced the formation of mammospheres in the micromolar range ^{21,60}.

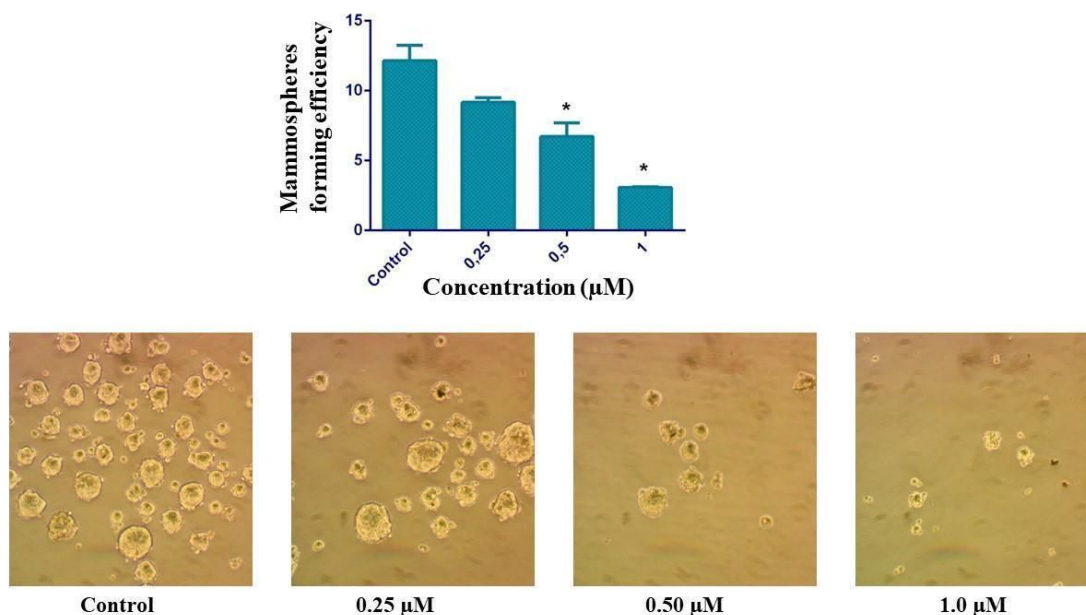


Figure 9. Mammospheres forming capacity. Mammospheres were incubated in Dulbecco's modified Eagle's medium (DMEM) alone (control) or with different concentrations (0.25-1 μM) of CuHL. The results are expressed as Mammospheres forming efficiency (Number of mammospheres forming / Number of mammospheres seeded) x 100) and represent the mean ± the standard error of the mean (SEM). *p < 0.01 differences between control and treatment.

Conclusions

A new copper(II) complex obtained by the reaction of the hydrazone of 4-methoxybenzohydrazide with *o*Va was synthesized and characterized. The crystal structure of the cationic complex was determined and it was found that Cu(II) ion is in a distorted square pyramidal coordination and has nitrate as a counterion. DFT calculated geometrical parameters and spectroscopic features are in good agreement with experimental data.

Solid state FT-IR, Raman, EPR solid spectra and solution UV-vis of the complex along with spectroscopic data for the unbonded ligand were recorded and analyzed. In addition, solid spectra are in agreement with the crystallographic results and calculations allowed a complete assignment of the vibrational spectra. During the assignment of vibration bands for the copper complex it was observed strong coupling between some modes. The calculated electronic spectrum of the complex agrees with the observed one, allowing the assignment

of experimental bands of the Cu(II) complex in solution. In most cases, more than one electronic transition was involved in each absorption band.

The anticancer activity and the mechanism of action of CuHL was examined in the frame of a multidisciplinary scientific proposal concerned with the development of copper(II) complexes with potential antitumor effects. In this sense, CuHL caused cytotoxicity in a concentration-dependent fashion on several cancer cell lines, showing stronger anticancer activity than CDDP on bone, lung, colorectal and particularly on breast cancer cells.

Docking and molecular dynamics studies predicted that the complex could interact with DNA. These results are confirmed by comet assay in which the compound induced a significant genotoxic effect in MCF7 and MDA-MB-231 cells from 0.5 to 1 μ M. Moreover, CuHL augments the ROS levels and conveys the breast cancer cell to apoptosis at 0.5 μ M. Besides, the compound diminished the amount of breast CSCs on MCF7 and MDA-MB-231 cells, reducing the percentage of CD44⁺/CD24⁻/low cells from 0.5 to 1.5 μ M. Finally, CuHL showed a IC₅₀ value 65-fold lower than CDDP on breast multicellular spheroids and reduced the size and number of mammospheres.

Taking into account the selectivity and anticancer activity of CuHL and the scarce options on the treatment of triple negative breast adenocarcinoma, our results indicate that this complex is an engaging candidate for potential antitumor therapies and it would be attractive to further test this complex in *in vivo* assays for breast cancer treatments.

Experimental

Material

MeBH and oVA (Sigma-Aldrich), HCl (Carlo Erba), Cu(NO₃)₂.6H₂O (Riedel de H en) and 96% EtOH (Soria), were used as purchased. High purity methanol (Carlo Erba) was used for the electronic spectroscopy measurements. Dulbecco's modified Eagle's m dium (DMEM) and TrypLE TM were purchased from Gibco (Gaithersburg, MD, USA), and fetal bovine serum (FBS) was purchased from Internegocios (Argentina). Tissue culture materials were purchased from Corning (Princeton, NJ, USA). Annexin V, fluorescein isothiocyanate (FITC), propidium iodide (PI), DHR123 and Dihydroetidium were from Invitrogen (Buenos Aires, Argentina). CD44 and CD24 antibodies were purchased by BD (USA)

Methods

Synthesis

The hydrazone was prepared according to the procedure reported in ²⁷. Equimolar amounts of EtOH solutions of both the ligand and the cupric salt were heated and stirred separately. The copper solution was dropwise added to the ligand solution, leading to a green solution after the reaction shown in scheme 2. The system was kept under mild heating and stirring for 30 minutes. It was let stand at room temperature for two weeks. The green needle-shaped crystals were filtered off, washed with cold ethanol and dried in desiccator. M. P. 272-274 °C. Anal. Calc. for C₁₆ H₁₉ Cu N₃ O₉: C: 41.69%, H: 4.15%, N: 9.12 %. Found: C: 41.48%, H: 4.00%, N: 9.01 %.



Scheme 2. Schematic representation of the reaction between MeBH0Va and copper nitrate.

Physicochemical analysis

Spectroscopic data

IR spectra were recorded with a FTIR Bruker EQUINOX 55 instrument, using the KBr pellet technique and in the 4000-400 cm⁻¹ range. A WITEC alpha 300 RA spectrophotometer was used

to measure the Raman spectra, with a laser excitation wavelength of 532 nm, an integration time of 60s and a 20x objective lens. The laser power was 15mW for both compounds. The electronic spectra were done with a Hewlett-Packard 8452-A spectrophotometer in 10 mm quartz cells. Melting point (M. P.) was obtained with a Bock Monoscop “M” instrument. X-band EPR spectra were recorded on powdered samples in a Bruker EMX spectrometer, equipped with a Bruker ER 036TM NMR-teslameter and an Agilent 53150A microwave frequency counter. The simulations of the EPR spectra were performed using the SimFonia program ⁶¹, and graphics were represented by the Kaleidagraph v3.5 program ⁶². Experimental parameters of the data collection: modulation amplitude 0.1 mT, time constant 81.92 ms, conversion time 327.68 ms, gain $6.32 \cdot 10^2$ and power 20 mW. Microwave frequencies: 9.7773 GHz (Figure 4).

X-ray diffraction data

The measurements were performed on an Oxford Xcalibur Gemini, Eos CCD diffractometer with graphite-monochromated $\text{CuK}\alpha$ ($\lambda = 1.54178 \text{ \AA}$) radiation. X-ray diffraction intensities were collected (ω scans with ϑ and κ -offsets), integrated and scaled with CrysAlisPro ⁶³ suite of programs. The unit cell parameters were obtained by least-squares refinement (based on the angular setting for all collected reflections with intensities larger than seven times the standard deviation of measurement errors) using CrysAlisPro. Data was corrected empirically for absorption employing the multi-scan method implemented in CrysAlisPro. The structure was solved by direct methods with SHELXS of the SHELX package ⁶⁴ and the molecular model developed by alternated cycles of Fourier methods and full-matrix least-squares refinement with SHELXL of the same suit of programs. All H-atoms but the water ones were positioned on a stereo-chemical basis and refined with the riding model. The waters H-positions were refined at their found positions with isotropic displacement parameters.

Crystallographic structural data have been deposited at the Cambridge Crystallographic Data Centre (CCDC). Any request to the Cambridge Crystallographic Data Centre for this material should quote the full literature citation and the reference numbers CCDC 1544958.

Computational methods

Taking the structural data obtained by x-ray diffraction methods as the starting point, the geometry of CuHL was optimized in the gas-phase using the hybrid density functional known

as B3LYP⁶⁵. The 6-311G** basis set was used for C, N, H and O⁶⁶, while the LANL2DZ pseudopotential was used for Cu⁶⁷.

The optimized geometry was characterized by the sign of the eigenvalues of the Hessian matrix of the total electronic energy with respect to the nuclear coordinates. When all the eigenvalues were positive, they were converted to harmonic vibrational frequencies.

Electronic transitions were calculated within the framework of the Time-Dependent DFT⁶⁸ using the PBE0 hybrid density functional⁶⁹. The 6-311+G(d,p) basis set was used for C, N, H and O^{66,70} and the same pseudopotential used for geometry optimization was used for Cu. Solvent effects (methanol) were included implicitly through the Conductor-like Polarizable Continuum Model⁷¹. Geometry optimizations, Hessian matrix calculation and diagonalization, and electronic transition calculations were performed with Gaussian 09 program⁷². The corresponding figures were done with wxMacMolPlt⁷³. Marvin was used for drawing, displaying and characterizing chemical structures, substructures and reactions, Marvin 20.14, 2020, ChemAxon (<http://www.chemaxon.com>).

Cell line and growth conditions

Human osteosarcoma cell line (MG-63), human lung cancer cell line (A549), breast cancer cell line (MCF-7 and MDA-MB-231), human colorectal cancer cell line (HT-29) and mouse non tumoral fibroblast (L929) were grown in Dulbecco's modified Eagle's medium (DMEM) containing 10% fetal bovine serum (FBS), 100 IU/mL penicillin and 100 µg/mL streptomycin at 37 °C in 5% CO₂ atmosphere. Human non tumoral breast cells (MCF10) was grown in DMEM F12 supplemented with 10 % FBS, 0.3 g/L glutamine, 20 ng/mL epidermal growth factor (EGF), 10 µg/mL insulin, 0.5 µg/mL hydrocortisone and 0.04 g/L gentamicin.

Cell viability study

The MTT assay was performed according to Mosmann et al⁷⁴. Briefly, cells were seeded in a 96-multiwell dish, allowed to attach for 24 h and treated with different concentrations of complex at 37 °C for 24 h. Afterward, medium was changed and cells were incubated with 0.5 mg/ml MTT under normal culture conditions for 3 h. Cell viability was marked by the conversion of the tetrazolium salt MTT (3-(4, 5-dimethylthiazol-2-yl)-2, 5-diphenyl-

tetrazoliumbromide) to a coloured formazan by mitochondrial dehydrogenases. Colour development was measured spectrophotometrically in a microplate reader (model 7530, Cambridge technology, Inc. USA) at 570 nm after cell lysis in DMSO (100 μ l/well). Cell viability was plotted as the percentage of the control value.

Clonogenic assay

Cells were seeded in 24 well plates, after attachment of the cells to the dishes, they were treated with CuHL at a range of 0,125 to 0,5 μ M. After 24 h, the cells were washed with PBS and 2 ml of complete DMEM were add. The plates were incubated for 10 days at 37°C and 5% CO₂. After this time, medium was removed, and cells were rinsed with PBS. Cells were stained with a mixture of 6% of glutaraldehyde and 0.5% of crystal violet for 30 minutes at room temperature. Then, the plates were washed with distilled water and dried. After, we proceed to count the colonies. The plating efficiency (PE) is the ratio of the number of colonies to the number of cells seeded whilst the number of colonies that survive after treatment, expressed in terms of PE, is called the surviving fraction (SF).

DNA studies

Computational methods

Structure preparation

The metal complex structure was drawn with Avogadro Molecular Editor⁷⁵. This coordinate served as a starting point for optimization via Density Functional Theory (DFT) calculation, which was carried out with the Gaussian 09 package⁷² using the B3LYP functional and 6-311G* and default parameters.

A dodecamer structure of the B-DNA duplex C-G-C-G-A-A-T-T-C-G-C-G was used as target sequence, and was taken from the Brookhaven Protein Data Bank⁷⁶. PDB ID: 1BNA⁷⁷. Water molecules were deleted from the structure and missing hydrogen atoms were added with UCSF Chimera molecular editor⁷⁸.

Molecular docking studies

Macromolecular docking was done using HEX 8.1 software ⁷⁹. In Hex's docking calculations, each molecule is modeled using 3D parametric functions which encode both surface shape and electrostatic charge. Hex docking reads DNA as a receptor file and complex as a ligand file from PDB-format.

The parameters used in the docking process were: correlation type: SHAPE-ELECTRO-DARS, FTT mode: 3D, grid dimension: 0.6, receptor range: -180, ligand range: -180, twist range: -360, distance range: 60, number of poses stocked: 10.

Molecular dynamics (MD)

MD simulation was performed on the best score pose of the metal complex in DNA resulting from molecular docking. The complex-DNA system has a negative net charge, so sodium cations were added as counterions with the Leap module to achieve electroneutrality. The neutralized complex was immersed in a box of TIP3P waters which extended up to 15 Å from the solute. DNA was described using the Amber14SB force field ⁸⁰. The metal complex CuHL was modeled with MCPB.py ⁸¹, included in the package AmberTools 19 ⁸². MD simulation was run using the NAMD 2.13 software ⁸³. The van der Waals interaction cutoff distances were set at 12 Å and long-range electrostatic forces were computed using the particle mesh Ewald summation method with a grid size set to 1.0 Å. The 1-4 contributions were multiplied by a factor of 0.83 to match the AMBER force field requirements. The system was subjected to 100000 minimization steps, heating from 0 to 300K in 30 ps, and 20 ns of equilibration/production simulation. For equilibration/production simulations, constant temperature (300 K) was maintained using Langevin dynamics with a damping coefficient of 5 ps⁻¹, while pressure was kept constant at 1 atm through the Nosé-Hoover Langevin piston method with a decay period of 200 fs and a damping time constant of 100 fs. A time step of 1 fs was used along molecular mechanics. Bonds involving hydrogen atoms of water were constrained using the SHAKE algorithm.

MM-GB/SA calculation

Binding free energy of CuHL with DNA was computed using the MM-GB/SA method, where the binding free energy is calculated as the difference between the bound and unbound state of DNA and metal complex ⁸⁴.

The solvation free energy was calculated using the generalized Born (GB) model ⁸⁵ implemented in MMPBSA.py module ⁸⁶, igb=2 as selected parameters. The hydrophobic contribution was determined using the solvent-accessible surface area (SASA). The DNA–metal complex binding free energy was calculated using a single trajectory based on 500 snapshots taken from the last 10 ns portion (20 ps interval) of the MD simulation trajectories. To obtain the detailed representation of interactions, free energy decomposition analysis was employed to decompose the total binding free energy into CuHL–nucleotide pairs. This calculation was performed using a pairwise energy decomposition scheme (idecomp option 3) also with the MMPBSA.py module.

Single cell gel electrophoresis (SCGE) assay

For detection of DNA strand breaks the single cell gel electrophoresis (‘comet’) assay was used in the alkaline version, based on the method of Singh et al with minor modifications ⁸⁷.

Under alkaline conditions, DNA loops containing breaks loose supercoiling, unwind and are released from the nuclei and form a ‘comet-tail’ by gel electrophoresis. For this experiment, 2×10^4 cells were seeded in a twelve-well plate; 24 h later the cells were incubated with concentrations of the complex (0.25–1 μM). After 24 h of treatment, cells were suspended in 0.5 % low melting point agarose and immediately poured onto glass microscope slides. Slides were immersed in ice-cold prepared lysis solution at darkness for 1 h (4°C) in order to lyse the cells, remove cellular proteins and to allow DNA unfolding. Immediately after, slides were put in a horizontal electrophoresis tank containing 1mM Na₂EDTA, 0.3M NaOH (pH 12.7) and then electrophoresis was performed for 30 min at 25V (4°C). Afterwards, slides were neutralized and stained with SyberGreen. Analysis of the slides was performed in an Olympus BX50 fluorescence microscope. Cellular images were acquired with the Leica IM50 Image Manager (Imagic Bildverarbeitung AG). A total of 50 randomly captured cells per experimental point of each experiment was used to determine the tail moment (product

of tail length by tail DNA percentage) using a free comet scoring software (Comet Score version 1.5).

Reactive Oxygen Species studies

Oxidative stress in MCF7 and MDA-MB-231 cells was evaluated by measurement of intracellular production of ROS after incubation of the cell monolayers with different concentrations of complex for 24 h at 37 °C. ROS generation was determined by oxidation of Dihydroethidium by spectrofluorimetry.

Apoptosis

Cells in early and late stages of apoptosis were detected with Annexin V-FITC and propidium iodide (PI) staining. Annexin V, fluorescein isothiocyanate (FITC), and propidium iodide (PI) Cells were treated with the CuHL for 24 h prior to analysis. For the staining, the cells were washed with PBS and were diluted with 1 μ L binding buffer. To 100 μ L of cell suspension, 2.5 μ L of Annexin V-FITC and 2 μ L PI (250 mg/mL) were added and incubated for 15 min at room temperature prior to analysis. Cells were analyzed using a flow cytometer BD Accuri C6 Plus and BD Accuri C6 Plus software. For each analysis 10 000 counts, gated on an FSC vs. SSC dot plot, were recorded.

Cancer Stem Cell studies

MCF7 and MDA-MB-231 cells were collected and monoclonal antibodies against human CD44-FITC and CD24PE (BD Biosciences, USA) were added to the cell suspension with the recommended concentration and incubated at room temperature in dark for 30 min. Then, the cells were washed with phosphate-buffered saline (PBS) and analyzed by the BD Accuri C6 Plus.

Multicellular tumor spheroid formation

Multicellular tumor spheroids were formed with MCF7 cells using the adapted hanging drop method⁸⁸. In brief, an aliquot of 25 μ l cell suspension containing 1500 cells was suspended on the lid of the cell culture plate. After the time-point required for cell aggregation (72 h),

the spheroids were transferred to agarose-coated 96-well plates (one droplet in one well) and cultured with 150 μ l culture medium. Spheroids were allowed to grow until reaching a size of 300 μ m diameter.

Spheroids cell viability study

Multicellular spheroids were treated in 96-well plates with 0.5% DMSO in DMEM (control) and with complex in a range of concentration 0.5 to 10 μ M in DMEM for 48 h. Afterward, cell viability of spheroids was evaluated by the resazurin reduction assay.

Spheroid clonogenic assay

Multicellular spheroids were treated in 96-well plates with 0.5% DMSO in DMEM (control) and with complex in a range of concentration 2.5 to 10 μ M in DMEM for 48 h.

Afterward, spheroids were dissociated enzymatically (10 min at 37°C in 0.05% trypsin), and mechanically by gently pipetting, and resuspended in DMEM with 10% FBS. Cells were then transferred to a 6-well plate (one spheroid per plate) and incubated for 7 days. After this time, cells were stained using a mixture of 6% glutaraldehyde and 0.5% crystal violet. The number of colonies formed was counted.

Spheroids spreading assay

Multicellular spheroids were treated in 96-well plates with 0.5% DMSO in DMEM (control) and with complex in a range of concentration 1 to 10 μ M in DMEM for 48 h.

Afterward, spheroids were transferred to a conventional 48-well plate and images were obtained after 48h, using an inverted microscope. Effects of the compound were analyzed by measuring the area covered by migration cells using ImageJ software.

Mammospheres formation

Single cells derived from MCF-7 cell line was plated in 12-well low attachment suspension culture plates at a density of 2000 viable cells/well. Cells were grown in 1000 mL serum-free media, supplemented with B27 and 20 ng/mL EGF as previously described⁵⁶. Mammospheres were counted after 5–8 days in culture with an Olympus IX20 inverted microscope.

Statistical analysis

Results are expressed as the mean of three independent experiments and plotted as mean \pm standard error of the mean (SEM). The total number of repeats (n) is specified in the legends of the figures. Statistical differences were analyzed using the analysis of variance method followed by the test of least significant difference (Fisher). The statistical analyses were performed using STATGRAPHICS Centurion XVII.I.

Author contributions

Conceptualization, LMB, VFC, AGB and IEL; methodology and practical chemical and spectroscopic studies, VFC and AGB ; crystallography, O.P and G.E.; EPR studies, JGT; theoretical calculations (DFT studies and DNA interaction), VFC, RPD, MJL; methodology on biological studies, LMB and IEL; writing, reviewing and editing VFC, AGB and IEL; project administration and funding acquisition, AGB and IEL.

Conflicts of interest

There are no conflicts to declare

Acknowledgments

This work was supported by CONICET (PIP 0340 and 0651), UNLP (X041 and X857) and ANPCyT (PICT 2016-1574), Argentina. A.C.G.B, G.A.E., M.J.L, I.E.L, O.E.P and R.P.D. are members of the Research Career of CONICET. V.F.C. is a member of the Technical Career of CONICET. LMB has a fellowship from CONICET. The authors thank the School of Exact and Natural Sciences, National University of Catamarca, Argentina for computing

time and Dr. David Ibáñez Martínez (Department of Chemistry, University of Burgos, Spain) for Raman spectra. The authors are grateful for the support of NVIDIA Corporation with the donation of the Titan X Pascal GPU used for this research.

Supplementary Material. Tables of full bond distances and angles (Table S1), fractional coordinates and equivalent isotropic displacement parameters of the non-H atoms (Table S2), atomic anisotropic displacement parameters (Table S3), hydrogen atoms positions (Table S4), hydrogen bond distances and angles (Table S5) and complete IR and Raman modes (Table S6).

References

- 1 L. A. Torre, F. Bray, R. L. Siegel, J. Ferlay, J. Lortet-Tieulent and A. Jemal, *CA. Cancer J. Clin.*, 2015, **65**, 87–108.
- 2 I. O. Alanazi and Z. Khan, *Asian Pac. J. Cancer Prev.*, 2016, **17**, 445–53.
- 3 S. Wen, L. Manuel, M. Doolan, J. Westhuyzen, T. P. Shakespeare and N. J. Aherne, *Breast Cancer Targets Ther.*, 2020, **12**, 27–35.
- 4 S. Al-Mahmood, J. Sapiezynski, O. B. Garbuzenko and T. Minko, *Drug Deliv. Transl. Res.*, 2018, **8**, 1483–1507.
- 5 P. Ferrari, A. Nicolini and A. Carpi, *Biomed. Pharmacother.*, 2013, **67**, 543–555.
- 6 C. Y. Lin, K. Q. Barry-Holson and K. H. Allison, *Histopathology*, 2016, **68**, 119–137.
- 7 J.-A. de la Mare, L. Contu, M. C. Hunter, B. Moyo, J. N. Sterrenberg, K. C. H. Dhanani, L. Z. Mutsvunguma and A. L. Edkins, *Recent Pat. Anticancer. Drug Discov.*, 2014, **9**, 153–75.
- 8 U. Ndagi, N. Mhlongo and M. Soliman, *Drug Des. Devel. Ther.*, 2017, **11**, 599–616.
- 9 T. C. Johnstone, K. Suntharalingam and S. J. Lippard, *Chem. Rev.*, 2016, **116**, 3436–86.
- 10 D. Wang and S. J. Lippard, *Nat. Rev. Drug Discov.*, 2005, **4**, 307–320.

- 11 I. Ott and R. Gust, *Arch. Pharm. (Weinheim)*, 2007, **340**, 117–126.
- 12 I. Leon, J. Cadavid-Vargas, A. Di Virgilio and S. Etcheverry, *Curr. Med. Chem.*, 2017, **24**, 112–148.
- 13 D. Denoyer, S. A. S. Clatworthy and M. A. Cater, in *Metallo-Drugs: Development and Action of Anticancer Agents*, eds. A. Sigel, H. Sigel, E. Freisinger and R. K. O. Sigel, De Gruyter, Berlin, Boston, 2018, vol. 18, 469–506.
- 14 V. Gandin, C. Ceresa, G. Esposito, S. Indraccolo, M. Porchia, F. Tisato, C. Santini, M. Pellei and C. Marzano, *Sci. Rep.*, 2017, **7**, 13936.
- 15 C. Santini, M. Pellei, V. Gandin, M. Porchia, F. Tisato and C. Marzano, *Chem. Rev.*, 2014, **114**, 815–62.
- 16 R. Alemón-Medina, M. Breña-Valle, J. L. Muñoz-Sánchez, M. I. Gracia-Mora and L. Ruiz-Azuara, *Cancer Chemother. Pharmacol.*, 2007, **60**, 219–28.
- 17 J. Cadavid-Vargas, I. Leon, S. Etcheverry, E. Santi, M. Torre and A. Di Virgilio, *Anticancer. Agents Med. Chem.*, 2016, **17**, 424–433.
- 18 X. Shi, Z. Chen, Y. Wang, Z. Guo and X. Wang, *Dalt. Trans.*, 2018, **47**, 5049–5054.
- 19 C. Shobha Devi, B. Thulasiram, R. R. Aerva and P. Nagababu, *J. Fluoresc.*, 2018, **28**, 1195–1205.
- 20 L. M. Balsa, M. C. Ruiz, L. Santa Maria de la Parra, E. J. Baran and I. E. León, *J. Inorg. Biochem.*, 2020, **204**, 110975.
- 21 C. Lu, A. Eskandari, P. B. Cressey and K. Suntharalingam, *Chem. - A Eur. J.*, 2017, **23**, 11366–11374.
- 22 M. R. Rodríguez, L. M. Balsa, J. Del Plá, J. García-Tojal, R. Pis-Diez, B. S. Parajón-Costa, I. E. León and A. C. González-Baró, *New J. Chem.*, 2019, **43**, 11784–11794.
- 23 Y. Burgos-Lopez, J. Del Plá, L. M. Balsa, I. E. León, G. A. Echeverría, O. E. Piro, J. García-Tojal, R. Pis-Diez, A. C. González-Baró and B. S. Parajón-Costa, *Inorganica Chim. Acta*, 2019, **487**, 31–40.
- 24 S. D. Joshi, D. Kumar, S. R. Dixit, N. Tigadi, U. A. More, C. Lherbet, T. M. Aminabhavi

- and K. S. Yang, *Eur. J. Med. Chem.*, 2016, **121**, 21–39.
- 25 A. K. Tanoli, Z. Khan, T. Kamal, M. Ali, M. Latif and Z. T. Maqsood, *Pak. J. Pharm. Sci.*, 2019, **32**, 103–108.
- 26 M. Taha, H. Naz, S. Rasheed, N. H. Ismail, A. A. Rahman, S. Yousuf and M. I. Choudhary, *Molecules*, 2014, **19**, 1286–1301.
- 27 V. Ferraresi-Curotto, G. A. Echeverría, O. E. Piro, R. Pis-Diez and A. C. González-Baró, *Spectrochim. Acta Part A Mol. Biomol. Spectrosc.*, 2015, **137**, 692–700.
- 28 L. J. Farrugia, *J. Appl. Cryst.*, 1997, **30**, 565.
- 29 K. Nakamoto, in: “Infrared and Raman Spectra of Inorganic and Coordination Compounds”, Sixth ed., J. Wiley & Sons, Inc., Hoboken, New Jersey (2009).
- 30 D. Lin-Vien, N.B. Colthup, W.G. Fately, J.G. Grasselli in: “Infrared and Raman Characteristic Frequencies of Organic Molecules”, Academic Press, Boston, 1999.
- 31 A. B. P. Lever, E. Mantovani and B. S. Ramaswamy, *Can. J. Chem.*, 1971, **49**, 1957–1964.
- 32 C. C. Addison and W. B. Simpson, *J. Chem. Soc.*, 1965, 598–602.
- 33 B. J. Hathaway and D.E. Billing, *Coord. Chem. Rev.* 1970, **5**, 143–207.
- 34 D. E. Billing, R. J. Dudley, B. J. Hathaway and A. A. G. Tomlinson, *J. Chem. Soc. A*, 1971, 691–696.
- 35 A. W. Addison, T. N. Rao, J. Reedijk, J. van Rijn and G. C. Verschoor, *J. Chem. Soc., Dalton Trans.*, 1984, 1349–1356.)
- 36 N. M. Ayoub, K. M. Al-Shami, M. A. Alqudah and N. M. Mhaidat, *Onco. Targets. Ther.*, 2017, **10**, 4869–4883.
- 37 M. R. Rodríguez, J. Del Plá, L. M. Balsa, I. E. León, O. E. Piro, G. A. Echeverría, J. García-Tojal, R. Pis-Diez, B. S. Parajón-Costa and A. C. González-Baró, *New J. Chem.*, 2019, **43**, 7120–7129.
- 38 A. I. Matesanz, E. Jimenez-Faraco, M. C. Ruiz, L. M. Balsa, C. Navarro-Ranninger, I. E. León and A. G. Quiroga, *Inorg. Chem. Front.*, 2018, **5**, 73–83.
- 39 M. L. Low, G. Paulus, P. Dorlet, R. Guillot, R. Rosli, N. Delsuc, K. A. Crouse and C.

- Policar, *BioMetals*, 2015, **28**, 553–566.
- 40 C. Lu, A. Eskandari, P. B. Cressey and K. Suntharalingam, *Chemistry*, 2017, **23**, 11366–11374.
- 41 M. A. F. A. Manan, M. I. M. Tahir, K. A. Crouse, R. Rosli, F. N. F. How and D. J. Watkin, *J. Chem. Crystallogr.*, 2011, **41**, 1866–1871.
- 42 Y. Gou, Y. Zhang, J. Qi, S. Chen, Z. Zhou, X. Wu, H. Liang and F. Yang, *Oncotarget*, 2016, **7**, 67004–67019.
- 43 W. Liao, M. A. McNutt and W.-G. Zhu, *Methods*, 2009, **48**, 46–53.
- 44 I. Garcia-Bosch and M. A. Siegler, *Angew. Chemie - Int. Ed.*, 2016, **55**, 12873–12876.
- 45 A. Sîrbu, O. Palamarcu, M. V. Babak, J. M. Lim, K. Ohui, E. A. Enyedy, S. Shova, D. Darvasiová, P. Rapta, W. H. Ang and V. B. Arion, *Dalt. Trans.*, 2017, **46**, 3833–3847.
- 46 S. Majumder, P. Dutta, A. Mookerjee and S. K. Choudhuri, *Chem. Biol. Interact.*, 2006, **159**, 90–103.
- 47 S. Y. Tsang, S. C. Tam, I. Bremner and M. J. Burkitt, *Biochem. J.*, 1996, **317 (Pt 1)**, 13–6.
- 48 F. R. M. Laurindo, D. C. Fernandes and C. X. C. Santos, in *Methods in Enzymology*, Academic Press Inc., 2008, vol. 441, 237–260.
- 49 C. N. Hancock, L. H. Stockwin, B. Han, R. D. Divelbiss, J. H. Jun, S. V Malhotra, M. G. Hollingshead and D. L. Newton, *Free Radic. Biol. Med.*, 2011, **50**, 110–21.
- 50 C. R. Kowol, P. Heffeter, W. Miklos, L. Gille, R. Trondl, L. Cappellacci, W. Berger and B. K. Keppler, *J. Biol. Inorg. Chem.*, 2012, **17**, 409–23.
- 51 M. Hassan, H. Watari, A. AbuAlmaaty, Y. Ohba and N. Sakuragi, *Biomed Res. Int.*, 2014, **2014**, 1–23.
- 52 M. C. Cabrera, R. E. Hollingsworth and E. M. Hurt, *World J. Stem Cells*, 2015, **7**, 27–36.
- 53 M. Z. Ratajczak, *Folia Histochem. Cytobiol.*, 2005, **43**, 175–81.
- 54 F. Islam, B. Qiao, R. A. Smith, V. Gopalan and A. K. Y. Lam, *Exp. Mol. Pathol.*, 2015, **98**, 184–191.

- 55 M. L. De Angelis, F. Francescangeli and A. Zeuner, *Cancers (Basel)*, 2019, **11**, 1569.
- 56 M. Al-Hajj, M. S. Wicha, A. Benito-Hernandez, S. J. Morrison and M. F. Clarke, *Proc. Natl. Acad. Sci. U. S. A.*, 2003, **100**, 3983–3988.
- 57 S. Roberts, S. Peyman and V. Speirs, in *Advances in experimental medicine and biology*, 2019, vol. 1152, 413–427.
- 58 G. Dontu and M. S. Wicha, *J. Mammary Gland Biol. Neoplasia*, 2005, **10**, 75–86.
- 59 K. Laws, G. Bineva-Todd, A. Eskandari, C. Lu, N. O'Reilly and K. Suntharalingam, *Angew. Chemie Int. Ed.*, 2018, **57**, 287–291.
- 60 P. Zheng, A. Eskandari, C. Lu, K. Laws, L. Aldous and K. Suntharalingam, *Dalt. Trans.*, 2019, **48**, 5892–5896.
- 61 WINEPR SimFonia v1.25, Bruker Analytische Messtechnik GmbH, 1996.
- 62 Kaleidagraph v3.5 Synergy Software, 2000.
- 63 CrysAlisPro, Rigaku Oxford Diffraction (2015), version 1.171.38.41.
- 64 G. M. Sheldrick, *Acta Crystallogr. Sect. A Found. Crystallogr.*, 2008, **64**, 112–122.
- 65 D. Becke, *J. Chem. Phys.* 1993, **98**, 5648–5652.
- 66 T. Clark, J. Chandrasekhar, G. W. Spitznagel and P. V. R. Schleyer, *J. Comput. Chem.*, 1983, **4**, 294–301.
- 67 P. J. Hay and W. R. Wadt, *J. Chem. Phys.*, 1985, **82**, 299–310.
- 68 A. Dreuw and M. Head-Gordon, *Chem. Rev.*, 2005, **105**, 4009–4037.
- 69 C. Adamo and V. Barone, *J. Chem. Phys.*, 1999, **110**, 6158–6170.
- 70 R. Krishnan, J. S. Binkley, R. Seeger and J. A. Pople, *J. Chem. Phys.*, 1980, **72**, 650–654.
- 71 M. Cossi, N. Rega, G. Scalmani and V. Barone, *J. Comput. Chem.*, 2003, **24**, 669–681.
- 72 Gaussian 09, Revision A.02, M. J. Frisch, G. W. Trucks, H. B. Schlegel, G. E. Scuseria, M. A. Robb, J. R. Cheeseman, G. Scalmani, V. Barone, G. A. Petersson, H. Nakatsuji, X. Li, M.

- Caricato, A. Marenich, J. Bloino, B. G. Janesko, R. Gomperts, B. Mennucci, H. P. Hratchian, J. V. Ortiz, A. F. Izmaylov, J. L. Sonnenberg, D. Williams-Young, F. Ding, F. Lipparini, F. Egidi, J. Goings, B. Peng, A. Petrone, T. Henderson, D. Ranasinghe, V. G. Zakrzewski, J. Gao, N. Rega, G. Zheng, W. Liang, M. Hada, M. Ehara, K. Toyota, R. Fukuda, J. Hasegawa, M. Ishida, T. Nakajima, Y. Honda, O. Kitao, H. Nakai, T. Vreven, K. Throssell, J. A. Montgomery, Jr., J. E. Peralta, F. Ogliaro, M. Bearpark, J. J. Heyd, E. Brothers, K. N. Kudin, V. N. Staroverov, T. Keith, R. Kobayashi, J. Normand, K. Raghavachari, A. Rendell, J. C. Burant, S. S. Iyengar, J. Tomasi, M. Cossi, J. M. Millam, M. Klene, C. Adamo, R. Cammi, J. W. Ochterski, R. L. Martin, K. Morokuma, O. Farkas, J. B. Foresman, and D. J. Fox, Gaussian, Inc., Wallingford CT, 2016.
- 73 B. M. Bode and M. S. Gordon, *J. Mol. Graph. Model.*, 1998, **16**, 133–138.
- 74 T. Mosmann, *J. Immunol. Methods*, 1983, **65**, 55–63.
- 75 M. D. Hanwell, D. E. Curtis, D. C. Lonie, T. Vandermeersch, E. Zurek and G. R. Hutchison, *J. Cheminform.*, 2012, **4**, 17.
- 76 P. W. Rose, B. Beran, C. Bi, W. F. Bluhm, D. Dimitropoulos, D. S. Goodsell, A. Prlić, M. Quesada, G. B. Quinn, J. D. Westbrook, J. Young, B. Yukich, C. Zardecki, H. M. Berman and P. E. Bourne, *Nucleic Acids Res.*, 2011, **39**, 392-401.
- 77 H. R. Drew, R. M. Wing, T. Takano, C. Broka, S. Tanaka, K. Itakura and R. E. Dickerson, *Proc. Natl. Acad. Sci. U. S. A.*, 1981, **78**, 2179–2183.
- 78 E. F. Pettersen, T. D. Goddard, C. C. Huang, G. S. Couch, D. M. Greenblatt, E. C. Meng and T. E. Ferrin, *J. Comput. Chem.*, 2004, **25**, 1605–1612.
- 79 L. Mavridis, B. D. Hudson and D. W. Ritchie, *J. Chem. Inf. Model.*, 2007, **47**, 1787–1796.
- 80 J. A. Maier, C. Martinez, K. Kasavajhala, L. Wickstrom, K. E. Hauser and C. Simmerling, *J. Chem. Theory Comput.*, 2015, **11**, 3696–3713.
- 81 P. Li and K. M. Merz, *J. Chem. Inf. Model.*, 2016, **56**, 599–604.
- 82 T. A. D. D.A. Case, I.Y. Ben-Shalom, S.R. Brozell, D.S. Cerutti, T.E. Cheatham, III, V.W.D. Cruzeiro, Y. H. R.E. Duke, D. Ghoreishi, M.K. Gilson, H. Gohlke, A.W. Goetz, D. Greene, R Harris, N. Homeyer, D. J. S. Izadi, A. Kovalenko, T. Kurtzman, T.S. Lee, S. LeGrand, P. Li, C. Lin, J. Liu, T. Luchko, R. Luo, R. Mermelstein, K.M. Merz, Y. Miao, G.

- Monard, C. Nguyen, H. Nguyen, I. Omelyan, A. Onufriev, F. Pan and D. M. Y. and P. A. K. Qi, D.R. Roe, A. Roitberg, C. Sagui, S. Schott-Verdugo, J. Shen, C.L. Simmerling, J. Smith, R. SalomonFerrer, J. Swails, R.C. Walker, J. Wang, H. Wei, R.M. Wolf, X. Wu, L. Xiao, .
- 83 J. C. Phillips, R. Braun, W. Wang, J. Gumbart, E. Tajkhorshid, E. Villa, C. Chipot, R. D. Skeel, L. Kalé and K. Schulten, *J. Comput. Chem.*, 2005, **26**, 1781–802.
- 84 Y. N. Vorobjev and J. Hermans, *Biophys. Chem.*, 1999, **78**, 195–205.
- 85 W. Clark Still, A. Tempczyk, R. C. Hawley and T. Hendrickson, *J. Am. Chem. Soc.*, 1990, **112**, 6127–6129.
- 86 B. R. Miller, T. D. McGee, J. M. Swails, N. Homeyer, H. Gohlke and A. E. Roitberg, *J. Chem. Theory Comput.*, 2012, **8**, 3314–21.
- 87 N. P. Singh, M. T. McCoy, R. R. Tice and E. L. Schneider, *Exp. Cell Res.*, 1988, **175**, 184–91.
- 88 I. E. León, J. F. Cadavid-Vargas, A. Resasco, F. Maschi, M. A. Ayala, C. Carbone and S. B. Etcheverry, *JBIC J. Biol. Inorg. Chem.*, 2016, **21**, 1009–1020.

**Anticancer activity of a new copper (II) complex with a hydrazone ligand.
Structural and spectroscopic characterization, computational simulations and cell
mechanistic studies on 2D and 3D breast cancer cell models**

Lucia M. Balsa¹, Verónica Ferraresi-Curotto^{2*}, Martin J. Lavecchia¹, Gustavo A. Echeverría², Oscar E. Piro², **Javier García-Tojal³**, Reinaldo Pis-Diez¹, Ana C. González-Baró¹, Ignacio E. León^{1*}

¹ Centro de Química Inorgánica (CEQUINOR, CONICET-UNLP), Facultad de Ciencias Exactas, Universidad Nacional de La Plata, Bv 120 1465, 1900 La Plata, Argentina

² Instituto de Física La Plata (IFLP, CONICET-UNLP), CC 67, B1900AVV, La Plata, Argentina

³ Departamento de Química, Universidad de Burgos, Plaza Misael Bañuelos s/n, 09001 Burgos, Spain

* ileon@biol.unlp.edu.ar, yfc@fisica.unlp.edu.ar

Supplementary Material

Table S1. Full bond lengths [Å] and angles [°] for [Cu(HL)(H₂O)₂].NO₃.

Bond lengths [Å]			
C(1)-C(6)	1.407(4)	C(11)-C(12)	1.381(4)
C(1)-C(2)	1.409(4)	C(12)-C(13)	1.385(5)
C(1)-C(8)	1.440(4)	C(13)-O(3)	1.348(4)
C(2)-O(1)	1.319(3)	C(13)-C(14)	1.385(5)
C(2)-C(3)	1.422(4)	C(14)-C(15)	1.375(4)
C(3)-O(4)	1.370(4)	C(16)-O(3)	1.432(5)
C(3)-C(4)	1.376(4)	N(1)-N(2)	1.384(3)
C(4)-C(5)	1.391(5)	N(1)-Cu	1.930(2)
C(5)-C(6)	1.364(5)	O(1)-Cu	1.889(2)
C(7)-O(4)	1.417(4)	O(2)-Cu	1.966(2)
C(8)-N(1)	1.286(4)	O(1W)-Cu	2.318(2)
C(9)-O(2)	1.256(3)	O(2W)-Cu	1.975(2)
C(9)-N(2)	1.343(4)	N(3)-O(33)	1.187(4)
C(9)-C(10)	1.471(3)	N(3)-O(32)	1.232(4)
C(10)-C(15)	1.392(4)	N(3)-O(31)	1.249(4)
C(10)-C(11)	1.395(4)		

Bond angles [°]			
C(6)-C(1)-C(2)	119.8(3)	C(12)-C(13)-C(14)	119.7(3)
C(6)-C(1)-C(8)	116.9(3)	C(15)-C(14)-C(13)	120.4(3)
C(2)-C(1)-C(8)	123.3(2)	C(14)-C(15)-C(10)	120.8(3)
O(1)-C(2)-C(1)	125.7(2)	C(8)-N(1)-N(2)	120.0(2)
O(1)-C(2)-C(3)	116.7(2)	C(8)-N(1)-Cu	128.1(2)
C(1)-C(2)-C(3)	117.6(2)	N(2)-N(1)-Cu	111.9(2)
O(4)-C(3)-C(4)	125.3(3)	C(9)-N(2)-N(1)	114.5(2)
O(4)-C(3)-C(2)	113.4(2)	C(2)-O(1)-Cu	126.1(2)
C(4)-C(3)-C(2)	121.3(3)	C(9)-O(2)-Cu	113.3(2)
C(3)-C(4)-C(5)	120.0(3)	C(13)-O(3)-C(16)	118.0(3)
C(6)-C(5)-C(4)	120.3(3)	C(3)-O(4)-C(7)	118.6(3)
C(5)-C(6)-C(1)	121.0(3)	O(1)-Cu-N(1)	93.51(9)
N(1)-C(8)-C(1)	123.1(2)	O(1)-Cu-O(2)	174.44(8)
O(2)-C(9)-N(2)	119.1(2)	N(1)-Cu-O(2)	81.10(9)
O(2)-C(9)-C(10)	120.4(2)	O(1)-Cu-O(2W)	91.61(9)
N(2)-C(9)-C(10)	120.4(2)	N(1)-Cu-O(2W)	158.4(1)
C(15)-C(10)-C(11)	118.3(2)	O(2)-Cu-O(2W)	92.93(9)
C(15)-C(10)-C(9)	118.1(2)	O(1)-Cu-O(1W)	90.75(9)
C(11)-C(10)-C(9)	123.5(3)	N(1)-Cu-O(1W)	107.75(9)
C(12)-C(11)-C(10)	121.0(3)	O(2)-Cu-O(1W)	92.20(9)
C(13)-C(12)-C(11)	119.8(3)	O(2W)-Cu-O(1W)	93.1(1)
O(3)-C(13)-C(12)	124.8(3)	O(33)-N(3)-O(32)	119.1(4)
O(3)-C(13)-C(14)	115.5(3)	O(33)-N(3)-O(31)	119.7(3)
		O(32)-N(3)-O(31)	121.1(3)

Table S2. Atomic coordinates (x 104) and equivalent isotropic displacement parameters (\AA^2 x 103) for $[\text{Cu}(\text{HL})(\text{H}_2\text{O})_2]\cdot\text{NO}_3$. $U(\text{eq})$ is defined as one third of the trace of the orthogonalized U_{ij} tensor.

atom	x	y	z	$U(\text{eq})$
C(1)	4235(4)	3246(3)	7176(2)	41(1)
C(2)	5163(4)	1979(3)	7545(2)	40(1)
C(3)	5890(4)	1246(3)	6758(2)	44(1)
C(4)	5758(5)	1765(3)	5668(2)	52(1)
C(5)	4864(5)	3023(3)	5321(2)	58(1)
C(6)	4094(5)	3745(3)	6059(2)	52(1)
C(7)	7474(7)	-810(4)	6495(3)	75(1)

C(8)	3430(4)	4091(2)	7886(2)	41(1)
C(9)	3035(4)	4203(2)	10589(2)	41(1)
C(10)	2265(4)	5018(2)	11359(2)	42(1)
C(11)	1514(4)	6307(3)	11034(2)	47(1)
C(12)	846(4)	7029(3)	11791(3)	51(1)
C(13)	887(4)	6468(3)	12893(3)	50(1)
C(14)	1616(5)	5187(3)	13227(3)	57(1)
C(15)	2317(5)	4474(3)	12468(3)	52(1)
C(16)	-562(5)	8399(4)	13410(4)	70(1)
N(1)	3513(3)	3763(2)	8916(2)	39(1)
N(2)	2727(3)	4628(2)	9548(2)	42(1)
O(1)	5429(3)	1408(2)	8561(2)	49(1)
O(2)	3976(3)	3098(2)	10900(2)	50(1)
O(1W)	2279(3)	1005(2)	10595(2)	53(1)
O(3)	277(4)	7081(2)	13700(2)	65(1)
O(2W)	6780(4)	879(2)	10517(2)	62(1)
O(4)	6724(4)	20(2)	7196(2)	58(1)
Cu	4741(1)	2158(1)	9758(1)	45(1)
N(3)	7943(4)	2278(2)	12271(2)	54(1)
O(31)	9054(4)	2830(3)	11473(2)	80(1)
O(32)	7864(7)	1179(3)	12378(3)	107(1)
O(33)	6878(8)	2833(4)	12913(3)	127(2)

Table S3. Anisotropic displacement parameters ($\text{\AA}^2 \times 10^3$) for $[\text{Cu}(\text{HL})(\text{H}_2\text{O})_2]\cdot\text{NO}_3$. The anisotropic displacement factor exponent takes the form: $-2\pi^2[h^2a^{*2}U^{11} + \dots + 2hk a^* b^* U^{12}]$.

atom	U^{11}	U^{22}	U^{33}	U^{23}	U^{13}	U^{12}
C(1)	43(1)	41(1)	38(1)	-11(1)	-4(1)	-11(1)
C(2)	46(1)	40(1)	37(1)	-11(1)	-5(1)	-13(1)
C(3)	52(1)	42(1)	41(1)	-14(1)	-6(1)	-11(1)
C(4)	60(2)	59(2)	38(1)	-21(1)	-4(1)	-10(1)
C(5)	70(2)	64(2)	34(1)	-9(1)	-9(1)	-7(2)

C(6)	60(2)	49(2)	41(1)	-6(1)	-10(1)	-4(1)
C(7)	113(3)	52(2)	63(2)	-32(2)	-9(2)	-6(2)
C(8)	46(1)	34(1)	41(1)	-8(1)	-8(1)	-5(1)
C(9)	49(1)	34(1)	44(1)	-14(1)	-8(1)	-10(1)
C(10)	47(1)	35(1)	48(1)	-19(1)	-7(1)	-7(1)
C(11)	52(1)	38(1)	51(2)	-14(1)	-9(1)	-7(1)
C(12)	52(1)	35(1)	67(2)	-22(1)	-8(1)	-2(1)
C(13)	46(1)	50(2)	62(2)	-31(1)	-7(1)	-9(1)
C(14)	72(2)	53(2)	49(2)	-19(1)	-16(1)	-4(1)
C(15)	67(2)	39(1)	52(2)	-16(1)	-15(1)	-4(1)
C(16)	61(2)	62(2)	99(3)	-53(2)	-9(2)	-2(2)
N(1)	46(1)	31(1)	42(1)	-13(1)	-6(1)	-6(1)
N(2)	51(1)	31(1)	44(1)	-15(1)	-8(1)	0(1)
O(1)	79(1)	33(1)	34(1)	-12(1)	-12(1)	-4(1)
O(2)	74(1)	33(1)	44(1)	-16(1)	-16(1)	1(1)
O(1W)	62(1)	42(1)	48(1)	-13(1)	-4(1)	-6(1)
O(3)	71(1)	63(1)	71(2)	-43(1)	-7(1)	-6(1)
O(2W)	89(2)	39(1)	63(1)	-20(1)	-35(1)	8(1)
O(4)	89(2)	39(1)	47(1)	-19(1)	-11(1)	-6(1)
Cu	68(1)	29(1)	38(1)	-13(1)	-13(1)	-3(1)
N(3)	68(2)	45(1)	43(1)	-13(1)	-15(1)	6(1)
O(31)	79(2)	69(2)	62(2)	-3(1)	-2(1)	10(1)
O(32)	167(4)	51(2)	106(3)	-15(2)	-53(3)	-9(2)
O(33)	174(4)	92(2)	90(3)	-48(2)	48(3)	-22(3)

Table S4. Hydrogen coordinates ($\times 10^4$) and isotropic displacement parameters ($\text{\AA}^2 \times 10^3$) for $[\text{Cu}(\text{HL})(\text{H}_2\text{O})_2]\cdot\text{NO}_3$.

atom	x	y	z	U(eq)
H(4)	6267	1273	5163	62
H(5)	4790	3374	4582	70
H(6)	3467	4580	5821	63
H(7A)	6428	-829	6151	113
H(7B)	7954	-1639	6918	113

H(7C)	8546	-524	5941	113
H(8)	2822	4913	7586	49
H(11)	1462	6686	10296	56
H(12)	370	7890	11561	61
H(14)	1630	4807	13968	69
H(15)	2832	3618	12700	63
H(16A)	375	8822	12851	105
H(16B)	-858	8728	14047	105
H(16C)	-1766	8531	13137	105
H(2)	2092	5377	9294	51
H(1A)	1250(40)	1510(30)	10820(30)	69(12)
H(1B)	2700(50)	500(30)	11168(17)	57(10)
H(2A)	7140(70)	890(40)	11090(20)	89(15)
H(2B)	7140(80)	131(19)	10450(40)	102(18)

Table S5. Hydrogen bond distances and angles in $[\text{Cu}(\text{HL})(\text{H}_2\text{O})_2]\cdot\text{NO}_3$.

D-H	d(D-H)	d(H..A)	$\angle(\text{D-H..A})$	d(D..A)	A	Symmetry operation
N2-H2	0.86	2.03	171.8	2.886(3)	O31	$[-x+1, -y+1, -z+2]$
O1W-H1A	0.85(1)	2.06(1)	171(4)	2.903(3)	O31	$[x-1, y, z]$
O1W-H1B	0.85(1)	2.21(2)	132(3)	2.847(3)	O1	$[-x+1, -y, -z+2]$
O1W-H1B	0.85(1)	2.14(2)	156(3)	2.936(3)	O4	$[-x+1, -y, -z+2]$
O2W-H2A	0.85(1)	1.99(1)	172(4)	2.839(5)	O32	

Table S6. Complete IR and Raman spectra of H_2L and $[\text{Cu}(\text{HL})(\text{H}_2\text{O})_2]\cdot\text{NO}_3$.

H_2L			$[\text{Cu}(\text{HL})(\text{H}_2\text{O})_2]^+$			
IR	Raman	Assignment	IR	Raman	Calculated	Assignment
3571 m		$\nu \text{H}_2\text{O}$	3396 m,b			$\nu \text{H}_2\text{O}_{\text{coord}}$
3213 m		νNH	3178 w,b		3539	νNH
3006 vw		νOH	—			νOH
3102 w		$\nu \text{CHip MeBH}$	3114 vw		3232	$\nu \text{CHip MeBH}$
3080 w	3083	$\nu \text{CHip oVa}$	3087		3217	$\nu \text{CHip oVa}$

2929 vw		$\nu_{as} \text{CH}_3 \text{ MeBH}$	3075 vw		3160/3090	$\nu_{as} \text{CH}_3 \text{ MeBH}$
2951 vw		$\nu_{as} \text{CH}_3 \text{ oVa}$	2985 vw		3142/5056	$\nu_{as} \text{CH}_3 \text{ oVa}$
2833 vw		νC8H	2948 vw		3030	νC8H
			2888		3025	$\nu_s \text{CH}_3 \text{ MeBH}$
2847 vw		$\nu_s \text{CH}_3 \text{ oVa}$	2855		3001	$\nu_s \text{CH}_3 \text{ oVa}$
			1767 vw			$\nu_1 + \nu_4 \text{NO}_3^-$
1650 s	1660 w	$\nu \text{C=O}$				
1608 s (b)	1610 vs	$\nu \text{C=N}$	1607 s	1609 vs	1688	$\nu \text{C=N} + \nu \text{C=O} + \nu \text{ring oVa}$
			1590 w	1590 sh	1666	$\nu \text{ring MeBH} + \text{Ar-C}$
1577 m	1581 s	$\nu \text{ring} + \text{Ar-OCH}_3 \text{ (MeBH} + \text{oVa)}$	1575 w	1564 m	1661	$\nu \text{ring oVa}$
					1589	$(\nu \text{ring} + \nu \text{Ar-OCH}_3) \text{ oVa}$
			1538 m	1543 sh	1648	$\nu \text{C=O} + \nu \text{ring MeBH}$
1514 m	1518 vw	$\nu \text{ring} + \text{Ar-C (MeBH)}$	1512 m	1516 w	1606	$\nu \text{ring MeBH} + \nu \text{coord ring}$
1476 m	1485 m-w	$\nu \text{C-NH} + \nu \text{ring} + \nu \text{Ar-OCH}_3 \text{ (oVa)}$		1494 w	1550	$\text{C-NH} + \text{Ar-OCH}_3 \text{ MeBH} + \delta \text{NH}$
1460 sh	1473 sh	$\nu \text{ring} + \nu \text{Ar-C (oVa)} + \nu \text{Ar-OH} + \delta \text{as CH}_3 \text{ oVa}$	1468 w		1519 1517	$\delta \text{as CH}_3 \text{ oVa}$ $\delta \text{as CH}_3 \text{ MeBH}$
1440 vw	1449 vw	$\nu \text{ring} + \delta \text{sim CH}_3 \text{ oVa} + \nu \text{C-NH} + \delta \text{NH}$	1434 m	1435 w	1506	$(\nu \text{ring} + \delta \text{sim CH}_3) \text{ oVa} + \delta \text{NH}$
1419 vw		$\delta \text{as CH}_3 \text{ (MeBH)}$	1424 sh		1505	$\delta \text{as CH}_3 \text{ MeBH}$
1398 vw	1389 vw	$\delta \text{as CH}_3 \text{ oVa}$			1501	$\delta \text{as CH}_3 \text{ oVa}$
1371 m	1369 vvw	δOH				
			1384 vs	1390 m	1473	$\nu \text{ring (oVa)} + \nu \text{Ar-O (oVa)} \text{ coord ring} + \nu_3 \text{NO}_3^-$
1337 sh	1344		1335 sh	1332 w	1369	$(\delta \text{CH} + \nu \text{ring}) \text{ oVa} + \delta \text{C8H}$
1327 m	1327 m	$\nu \text{ring (oVa)} + \nu \text{Ar-OH}$	1319 sh		1366	$\delta \text{NH} + \delta \text{C8H} + \nu \text{ring (MeBH)}$
1315 m	1320 sh	$\delta \text{CH} + \nu \text{as N-C(O)-C} + \nu \text{OH}$	1304 w	1308 vw	1298	$\delta \text{C8H} + \nu \text{Ar-C MeBH}$

1296 m	1300 m	(ν C-OCH ₃ + ν ring) MeBH	1272 mw		1310	(ν C-OCH ₃ + ν ring) MeBH
	1268 sh					
1252 s	1259 w 1235 w	(ν C-OCH ₃ + δ ring) oVA	1247 m		1284	(ν C-OCH ₃ + δ ring) oVA
1182 m	1186 w	ν ring + ν Ar-OCH ₃ (oVa)				
1124 sh	1130 vw	δ C8H + ν ring (oVa)	1217 s		1243	δ C8H + ν ring (oVa)
1150 w		ρ_r CH ₃ + δ CH (oVa)			1221	ρ_r CH ₃ oVa
					1212	ρ_r CH ₃ MeBH
1168 w	1161 w	ν N-N + δ CH + ν_{as} NNC	1186 w	1192 sh	1158	ν N-N + δ CH (rings)
			1177 w	1179 w	1140	ν N-N + δ CH MeBH
1122 w	1220 vw	δ CH (MeBH)				
1106 sh 1098 w	1111 sh 1103 w	ν C-O(OCH ₃) + δ ring breath (MeBH)	1125 w	1111 vw	1070	(ν C-O(OCH ₃) + δ ring) MeBH
1080 w	1087 w	ν C-O(OCH ₃) + δ ring (oVa)	1083 w		1118	(ν C-O(OCH ₃) + δ ring) oVa
1065 m	1066 vvw					
			1036 sh	1043 w	1001	(ν C-O(OCH ₃) + δ ring) oVa
1035 m	1038 vw	δ ring (MeBH)	1023 m			δ ring MeBH
967 m 958 w		γ CH + γ_{ring} (MeBH)	977 w 972 sh	981 vvw	989	γ CH MeBH
893 m	899 w	γ CH (oVa)	906 w 885 vvw		956	γ C8H + ring (oVa)
893 m	899 w	γ CH (oVa)	856 sh		875	γ C8H + ring (oVa)
850 s		γ CH (MeBH)	846 m		863	γ CH MeBH
836 m	839 w	γ OH				
794 w 760 w	768 vw	γ CH + γ ring + γ CO (MeBH)				
736 s		γ CH + δ ring (oVa)	743 m		870	δ ring oVA
					814	δ ring MeBH
680 w	680 vw	δ N-N-C + γ C8H	648 w	644 vvw	916	δ coord. ring
610 m		γ NH	625 m	625	482	γ NH

				vvw	
			546 vw		570/541 v Cu-O
472 vw	476 vw	γ NH	482 vw		γ NH
			436 vw, b		γ NH + v N-Cu
418 vw		δ Ar-O-CH ₃ + δ C(O)-NH-N	416 vw		δ Ar-OCH ₃ + δ C(O)-NH-N

Calculated frequencies are not scaled. vs: very strong; s: strong; m: medium; w: weak; vw: very weak; vvw: very,very weak; sh: shoulder. v: stretching; δ : in-plane deformation; γ : out-of-plane deformation; pr: rocking. coord.ring = N-N-C=O-Cu

Table S7. Electronic absorption spectra of 3×10^{-5} M methanolic solution of the ligand and Cu complex. Results from TD-DFT are also shown. Percentage contributions of calculated transitions are given in parentheses. Absorption maxima are given in nm. Oscillator strengths, shown in parenthesis, are in a.u.

H ₂ L	[Cu(HL)(H ₂ O) ₂] ⁺		
Experimental	Experimental	Calculated	Assignment
			HOMO-1→LUMO+5 (24%) HOMO-1→LUMO+6 (16%) 251 (0.1246) HOMO→LUMO+6 (13%) Intra-ligand transition
220	230 sh (1.95x10 ⁵)	256 (0.0804)	HOMO-6→LUMO+1 (12%) HOMO-4→LUMO+1 (47%) Intra-ligand transition
260 sh	290 sh (1.11x10 ⁵)	279 (0.1612)	HOMO-7→LUMO (45%) HOMO-6→LUMO (26%) HOMO-4→LUMO (11%) Intra-ligand transition Charge transfer transition (L→M)
310			HOMO-7→LUMO (34%) HOMO-6→LUMO (19%) HOMO-4→LUMO (34%) Intra-ligand transition Charge transfer transition (L→M)
330 sh	322 (1.20x10 ⁵)	306 (0.2182)	
	402 (1.22x10 ⁵)	334 (0.1389)	HOMO-2→LUMO (16%) HOMO-1→LUMO+1 (56%) Charge transfer transition (L→M)

		340 (0.4314)	HOMO→LUMO+1 (20%) HOMO-2→LUMO (77%)	Charge transfer transition (L→M)
	710* (125.9)	532 (0.0039)	HOMO→LUMO (27%)	d → d

(L→M): Ligand to Metal

*found using a more concentrated solution of the complex ($1 \times 10^{-3} \text{M}$).

Figure S1. Drawings of Molecular orbitals most involved in electronic transitions.

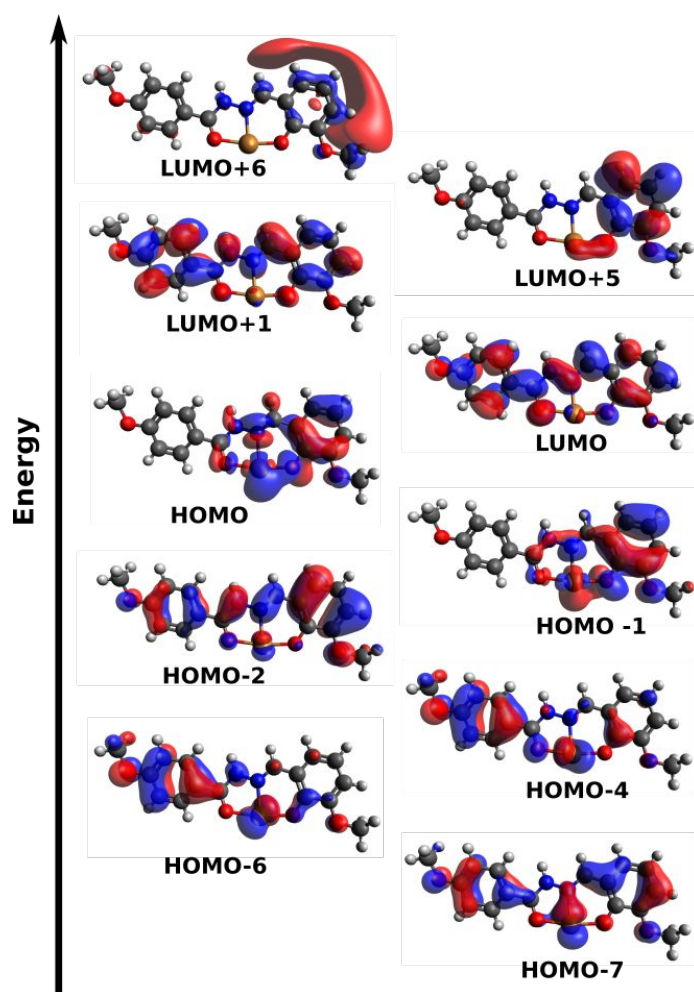


Figure S2. Root-mean-square deviation (RMSD) of dodecamer (blue line) and **CuHL** complex (red line) versus the dynamics simulation time.

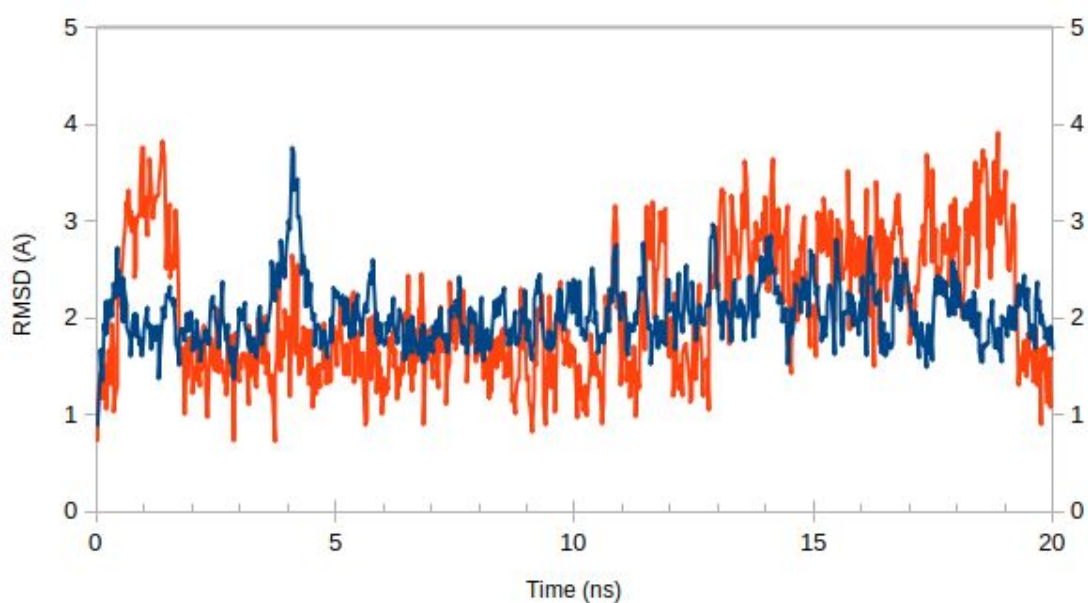


Figure S3. Energy decomposition of **CuHL** with nucleotides, based on molecular dynamics trajectory and using MM/GBSA model: total energy (green), interaction with Cu(II) (red) and interaction with the ligand (yellow). The original 1BNA PDB numbering was respected.

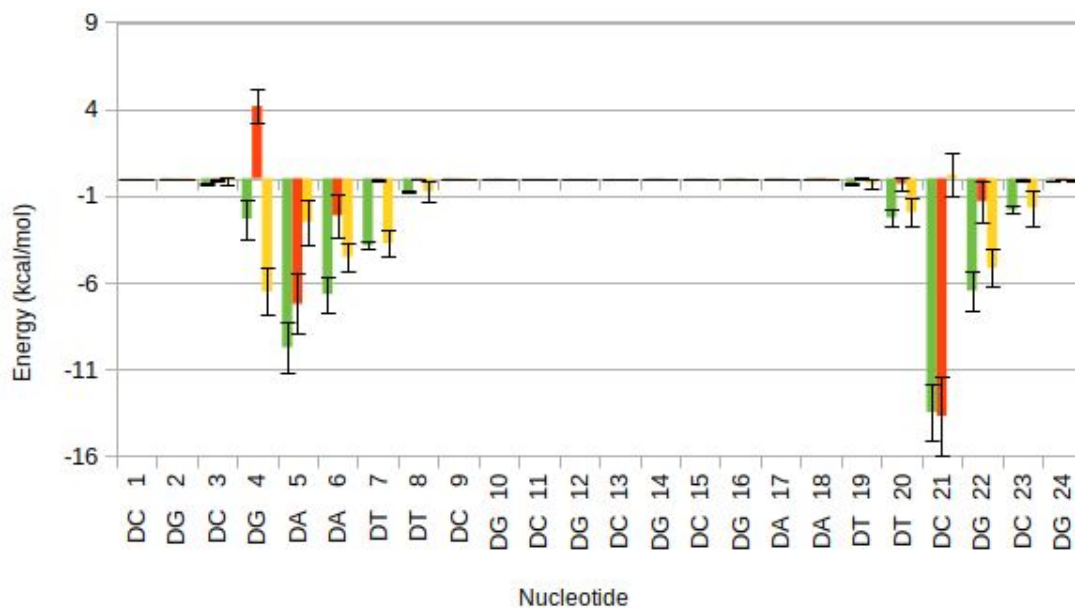


Figure S4 Apoptosis assay. The plots are representative of three independent experiments.

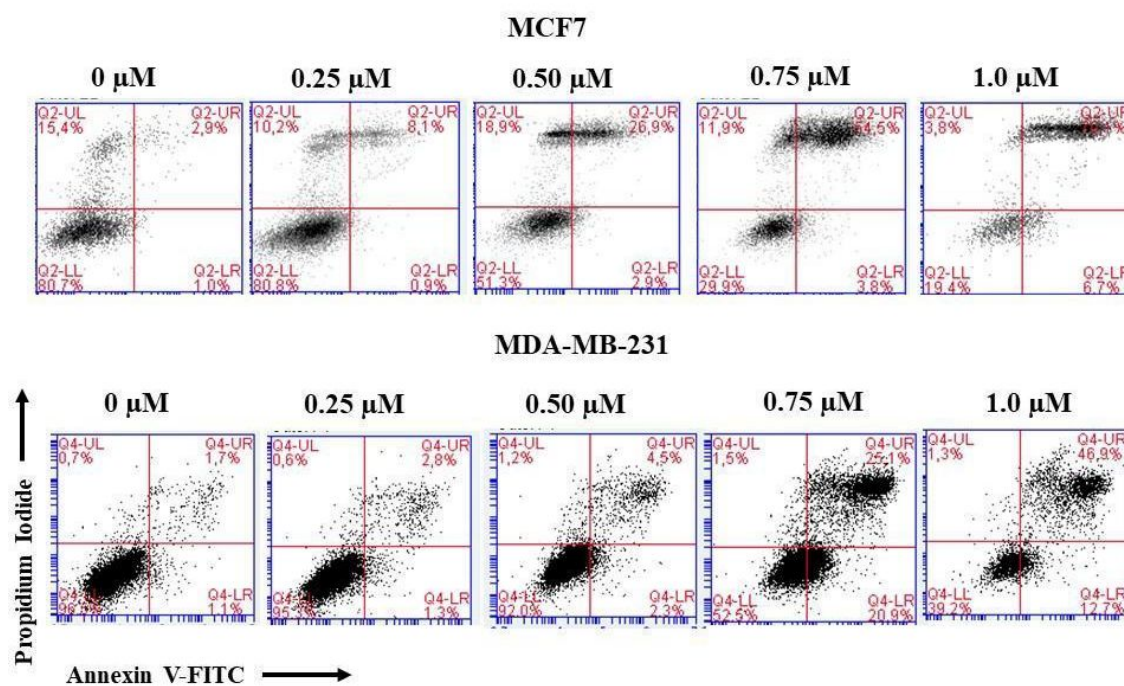


Figure S5 Cancer Stem Cell studies. The plots are representative of three independent experiments.

